Article

Metastatic medulloblastoma remodels the local leptomeningeal microenvironment to promote further metastatic colonization and growth

A list of authors and their affiliations appears at the end of the paper

Leptomeningeal metastases are the major source of morbidity and mortality for patients with medulloblastoma. The biology of the leptomeningeal metastases and the local tumour microenvironment are poorly characterized. Here we show that metastasis-associated meningeal fibroblasts (MB-MAFs) are transcriptionally distinct and signal extensively to tumour cells and the tumour microenvironment. Metastatic cells secrete platelet-derived growth factor (PDGF) ligands into the local microenvironment to chemotactically recruit meningeal fibroblasts. Meningeal fibroblasts are reprogrammed to become MB-MAFs, expressing distinct transcriptomes and secretomes, including bone morphogenetic proteins. Active bone morphogenetic protein signalling and co-implantation of tumour cells with MB-MAFs enhances the colonization of the leptomeninges by medulloblastoma cells and promotes the growth of established metastases. Furthermore, treatment of patient-derived xenograft mice with a PDGF-receptor-α neutralizing antibody enhances overall survival in vivo. Collectively, our results define a targetable intercellular communication cascade in the metastatic niche to treat leptomeningeal disease.

Medulloblastoma (MB) is the most prevalent malignant brain tumour in children. Developmentally, these tumours consist of a group of related embryonic malignancies of the hindbrain arising from various elements of the glutamatergic lineage rhombic lip[1-5]. Current multimodal treatment includes microneurosurgery, radiation of the entire brain and spinal cord, and cytotoxic chemotherapies[6,7]. No biological or targeted therapies are approved for treatment of children afflicted with either primary or metastatic MB, due at least in part to the lack of recurrent somatic mutations in targetable proteins.

Most deaths among patients with MB are secondary to metastatic disease[8]. Radiation of the entire craniospinal axis is often effective, but comes at a cost of damage to the developing nervous system[9,10]. Metastases are therefore the most common and most important source of both morbidity and mortality for children with MB[11]. MB metastasizes almost exclusively to the leptomeninges, although the mechanisms behind this exquisite selectivity are largely unknown[12]. Comparison of the transcriptomes of primary tumour cells and metastatic cells demonstrates dramatic transcriptional divergence[13,14], illustrating different biological and transcriptional states in distinct microenvironments. The multistep mechanisms by which a given primary tumour cell becomes a MB metastasis are poorly understood. For example, the route of tumour spread to the leptomeninges, which could include tumour cells shedding into the cerebrospinal fluid versus tumour cell hematogeneous spread, is an area of active investigation[15,16].

The leptomeninges are a harsh metabolic environment, bathed only in nutrient-poor cerebrospinal fluid, in contrast to the vascularized brain and spinal cord environments[17-19]. Based on this background, we hypothesized that tumour cells capable of forming leptomeningeal

✉e-mail: mdt.cns@gmail.com
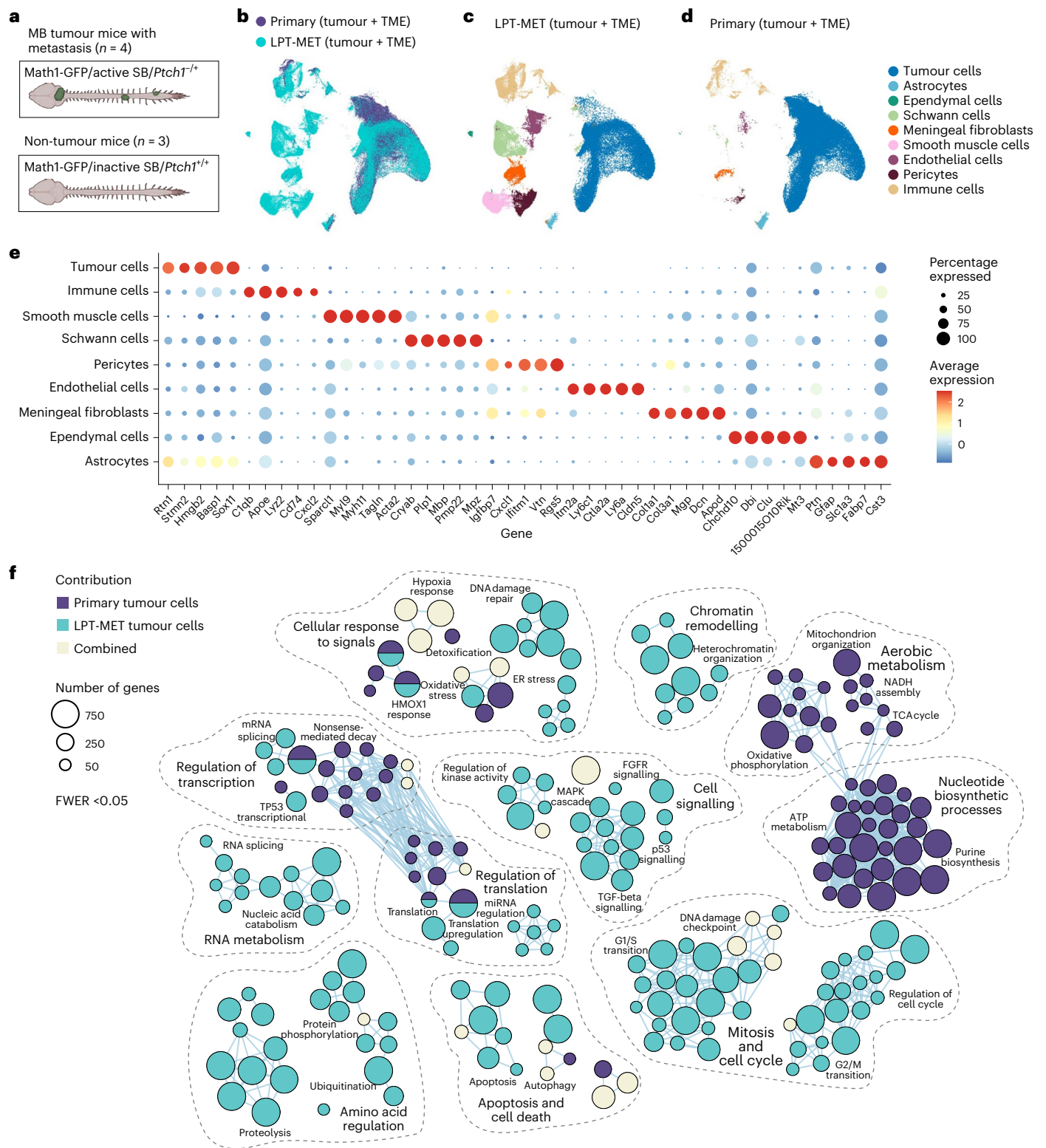
Fig. 1 | MB primary and metastatic tumour cells are functionally distinct.
a, A schematic representation of mouse Ptch-SB primary tumour and spinal leptomeninges with metastasis ($n = 4$ mice) and Ptch-WT non-tumour spinal leptomeninges ($n = 3$ mice) collected for scRNA-seq. **b**, UMAP plot of cells from Ptch-SB cerebellar primary tumours with TME denoted as primary (tumour + TME), and spinal leptomeninges with metastasis denoted as LPT-MET (tumour + TME). **c**,**d**, UMAP plots of annotated cell populations from LPT-MET (tumour + TME) samples (**c**) and primary (tumour + TME) samples (**d**). **e**, A dot plot with expression across cell types of the top five markers by log fold change (MAST test, log fold change (LFC) >0.25, minimum percent expression >0.1). **f**, Gene Ontology (GO) terms associated with genes differentially expressed in primary and LPT-MET tumour cells. The circle sizes correspond to the number of differentially expressed genes found in each pathway (Holm FWER <0.05). See Supplementary Table 1 for the full gene list and pathways. ER, endoplasmic reticulum.

metastases must initially establish a supportive microenvironment to colonize the leptomeninges and then clonally expand into bona fide metastases. Investigation into the specific molecular signalling mechanisms that promote the formation of a metastatic ecosystem within the leptomeninges might inform therapeutic strategies to prevent or treat metastatic MB in children.

Results

MB primary and metastatic cells are functionally distinct

Patched-1-heterozygous mutant mice (*Ptch1*^{+/−}) with *Sleeping Beauty* (SB) transposon-mediated mutagenesis are an immune-competent genetically engineered model of MB with leptomeningeal metastases (*Math1-GFP*/active SB/*Ptch1*^{+/−} or Ptch-SB)[13,20]. The normal leptomeninges consist of the cells from the pia mater, the arachnoid mater and enfolded cell types of the leptomeningeal vasculature[21,22]. To study leptomeningeal metastases, post-mortem spinal leptomeninges from Ptch-SB animals were isolated by shallowly incising the pia mater along the long axis of the spinal cord, and subsequently microdissecting the leptomeninges away from the neuronal contents of the spinal cord (Supplementary Fig. 1). Isolation of the leptomeninges allows imaging of the entire leptomeningeal axis, as well as single-cell RNA sequencing (scRNA-seq) that focuses exclusively on leptomeningeal cell types, minimizing contamination by the more numerous neurons and glia of the spinal cord proper.

Primary tumour and spinal leptomeningeal dissections from Ptch-SB tumour-bearing mice with metastases and control leptomeninges from non-tumour-bearing mice were isolated for scRNA-seq (Fig. 1a). We first compared the transcriptomic data of 65,086 single cells from primary tumours and associated microenvironments, denoted as primary (tumour + tumour microenvironment (TME)), to 76,477 single cells from the spinal leptomeninges with metastases, denoted as LPT-MET (tumour + TME) (Fig. 1b). We observed a higher proportion of cells from the TME in the LPT-MET samples compared with primary tumour samples. Within both primary tumour and LPT-MET samples, we identified nine distinct, major cell clusters (Fig. 1c,d), including tumour cells, astrocytes, ependymal cells, Schwann cells, meningeal fibroblasts, smooth muscle cells, endothelial cells, pericytes and immune cell populations (Fig. 1e)[23,24].

Comparison of single-cell transcriptional programs between pure primary tumour cells (which are less contaminated with TME cells) versus pure metastatic tumour cells revealed disparate cell-autonomous transcriptional programs with a switch from aerobic metabolism and nucleotide biosynthesis in primary tumours to amino acid metabolism in metastases (Fig. 1f, Extended Data Fig. 1a, b and Supplementary Table 1), suggesting a shift in metabolic states. LPT-MET tumour cells also differentially expressed genes associated with the cell cycle and growth factor signalling (Extended Data Fig. 1b). Thus, cell-autonomous tumour transcriptomes differ between the primary and metastatic MB compartments, as previously published[13].

Pathway enrichment analysis of genes differentially expressed between primary tumours and metastases support a model in which the TME is distinct between primary MB and leptomeningeal metastases. Thus, we interrogated the niche-specific intercellular signalling by CellChat[25]. In the primary tumour, the tumour cells are the most active cell type in both 'outgoing' and 'incoming' intercellular signalling (Extended Data Fig. 2a). By contrast, intercellular signalling in LPT-MET samples was predominant between the TME and the tumour cells, or between distinct cell types of the TME (Extended Data Fig. 2b). We hypothesized that intercellular signalling between the metastatic tumour cells and the various cellular constituents of the TME might promote the colonization of the leptomeninges and the subsequent growth of metastatic MB.

Meningeal fibroblasts as a major source of signalling

The metastatic process is complex and requires multiple steps for colonization of new tumour sites. To determine potential

molecular mechanisms by which tumour cells promote a hospitable niche within the leptomeninges, we compared the cell types in healthy, non-tumour-bearing leptomeninges (LPT-WT) and tumour-associated leptomeninges (LPT-MET). Although leptomeningeal metastases can occur at intracranial and spinal locations, we focused our analysis on the spinal leptomeninges. Single-cell transcriptomic data for 39,860 cells from LPT-WT and the 76,477 cells from LPT-MET were compared, revealing the presence of distinct cell types (Fig. 2a–c). All eight microenvironment cell types interacted with tumour cells and one another upon CellChat analysis (Fig. 2d), supporting a complex ecosystem in the metastatic niche. However, meningeal fibroblasts exhibited the strongest intercellular communication to metastatic tumour cells and the TME (Fig. 2e and Extended Data Fig. 3a).

We then interrogated the anatomical relationships between GFP-labelled tumour cells within the spinal leptomeninges and specific TME cell types in the Ptch-SB model. Although the degree and distribution of leptomeningeal metastases can vary between mice, GFP-labelled metastatic tumour cells can be found along the entire rostral–caudal extent of the spinal cord and in close physical relationship to the leptomeningeal blood vessels (Fig. 2f). The metastatic tumour cells reside in an extracellular matrix (ECM)-rich TME, surrounding both larger and smaller networks of vessels (Fig. 2g). Meningeal fibroblasts and oligodendrocyte precursor cells are known to express platelet-derived growth factor (PDGF) receptor α (PDGFRα)[23,26]. We confirmed that *Pdgfra* was expressed in the meningeal fibroblasts, along with the known meningeal fibroblast markers *Col1a1*, *Dcn* and *Lum* (Extended Data Fig. 4a–d). Oligodendrocyte precursor cell markers, *Olig1* and *Olig2*, were nearly absent in our scRNA-seq data, with the exception of a few metastatic tumour cells (Extended Data Fig. 4e,f). As a proportion of metastatic tumour cells express *Pdgfra* (Extended Data Fig. 4a), we excluded the PDGFRα and GFP double-positive tumour cells from subsequent analyses. We visualized the meningeal fibroblasts through *Pdgfra-H2BeGFP* reporter mice[27]. Meningeal fibroblasts surround leptomeningeal blood vessels and are also found attached to the pia mater or arachnoid mater (Fig. 2h). Indeed, the distribution of meningeal fibroblasts mirrored the distribution of metastatic tumour cells (Fig. 2g,h). This close spatial approximation of metastatic tumour cells and meningeal fibroblasts support the relevance of the intercellular signalling relationships identified at a transcriptional level by CellChat. We also found that the metastatic leptomeninges contain more PDGFRα-positive meningeal fibroblasts (Fig. 2i,j) and were more proliferative than fibroblasts from healthy leptomeninges (Fig. 2k).

We also compared meningeal fibroblasts from high versus low regions of patient-derived tumour xenografts, demonstrating increased proliferative indices of high tumour burden meningeal fibroblasts as measured by Ki67 (Fig. 3a). To determine the potential molecular mechanisms by which metastatic tumour cells influence meningeal fibroblasts, we compared intercellular signalling networks between metastatic tumour cells and meningeal fibroblasts. PDGF signalling appeared to signal from the metastatic tumour cells to the meningeal fibroblasts (Fig. 3b). To test the causative role of PDGF signalling, we overexpressed the secreted ligand PDGFA in the group 3 MB line, D458, showing that PDGFA secreting D458 clones recruited more meningeal fibroblasts than vector control tumour cells but did not affect fibroblast proliferation (Fig. 3c). We also showed that, when PDGFA was overexpressed, tumour cells were more proliferative (Fig. 3d) and the overall survival of mice was reduced in vivo (Fig. 3e). Thus, tumour cells secreting PDGFA, which diffuses into the local microenvironment, recruit additional meningeal fibroblasts to the metastatic niche, ultimately increasing tumour proliferation and reducing overall survival in vivo.

LPT-MET fibroblasts are transcriptionally distinct

To define the transcriptional heterogeneity between meningeal fibroblasts in the metastatic niche, we compared the scRNA-seq data
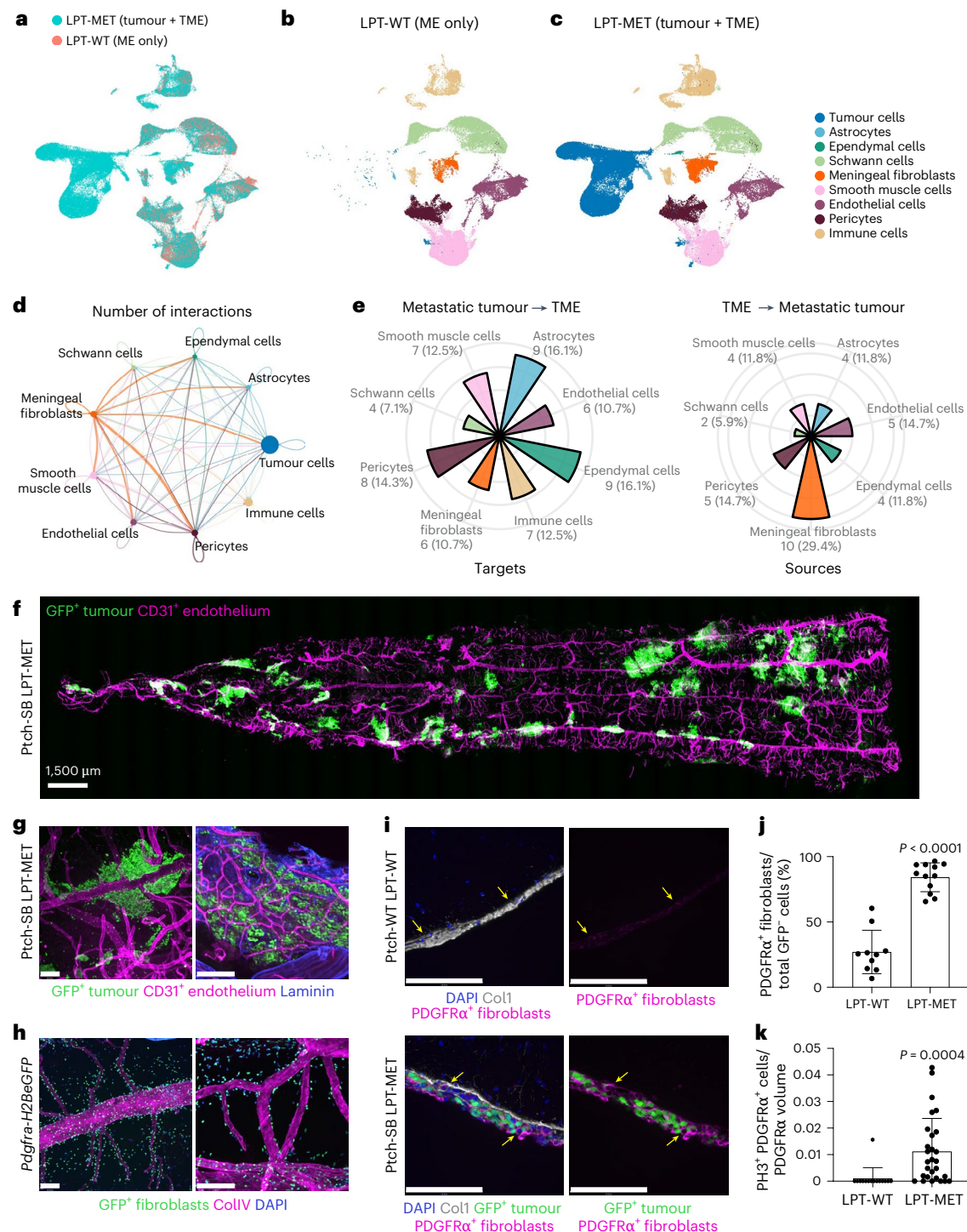
Fig. 2 | Distinct microenvironment signalling in the metastatic leptomeninges.
a, UMAP plot of cells from Ptch-WT control leptomeninges denoted as LPT-WT (ME only) and Ptch-SB leptomeninges with metastasis denoted as LPT-MET (tumour + TME). **b,c**, UMAP plots of annotated cell populations from LPT-WT (ME only) (**b**) and LPT-MET (tumour + TME) (**c**). **d**, Interaction plot of LPT-MET samples (the edge width represents the number of significant ligand–receptor pairs between any two cell populations, and the circle sizes represent the number of cells in each population). **e**, Detailed pie charts showing the proportion of interactions from the metastatic cells to the TME (left) and from the TME to the metastatic cells (right). **f,g**, Whole-mount Ptch-SB spinal leptomeninges with metastasis (LPT-MET) fluorescently labelled with GFP⁺ tumour and CD31⁺ endothelium (scale bar, 1,500 μm) (**f**) and GFP⁺ tumour, CD31⁺ endothelium and laminin with tumour cells associating with larger meningeal blood vessels (left) and a smaller network of vessels (right) (n = 47 images) (**g**). **h**, Representative whole-mount spinal leptomeninges from a *Pdgfra-H2BeGFP* reporter mouse

fluorescently labelled with GFP⁺ meningeal fibroblasts, collagen IV (ColIV) basement membrane and DAPI. Fibroblasts are found in the extracellular space and surround blood vessels (left). At a higher magnification, fibroblasts are shown to closely associate with blood vessels (right) (n = 15 images). **i**, Spinal cord cross-sections of Ptch-WT LPT-WT and Ptch-SB LPT-MET fluorescently labelled with collagen I (Col1), PDGFRα⁺ fibroblasts, GFP⁺ tumour and DAPI. The left panels show the merge, and the right panels show the GFP and PDGFRα channels (yellow arrows highlight PDGFRα⁺ GFP⁻ fibroblasts). **j**, The proportion of PDGFRα⁺ fibroblasts (PDGFRα⁺ GFP⁻ cells) per field of view (n = 10 and n = 12 images for LPT-WT and LPT-MET, respectively). **k**, Phospho-histone H3 (PH3) and PDGFRα double-positive fibroblasts normalized to PDGFRα volume quantified per field of view (n = 15 and n = 28 images for LPT-WT and LPT-MET, respectively). P values were generated from two-tailed unpaired t-test with Welch's correction, the centre line represents the mean and error bars represent the standard deviation for **j** and **k**. Scale bars, 120 μm (**g–i**).
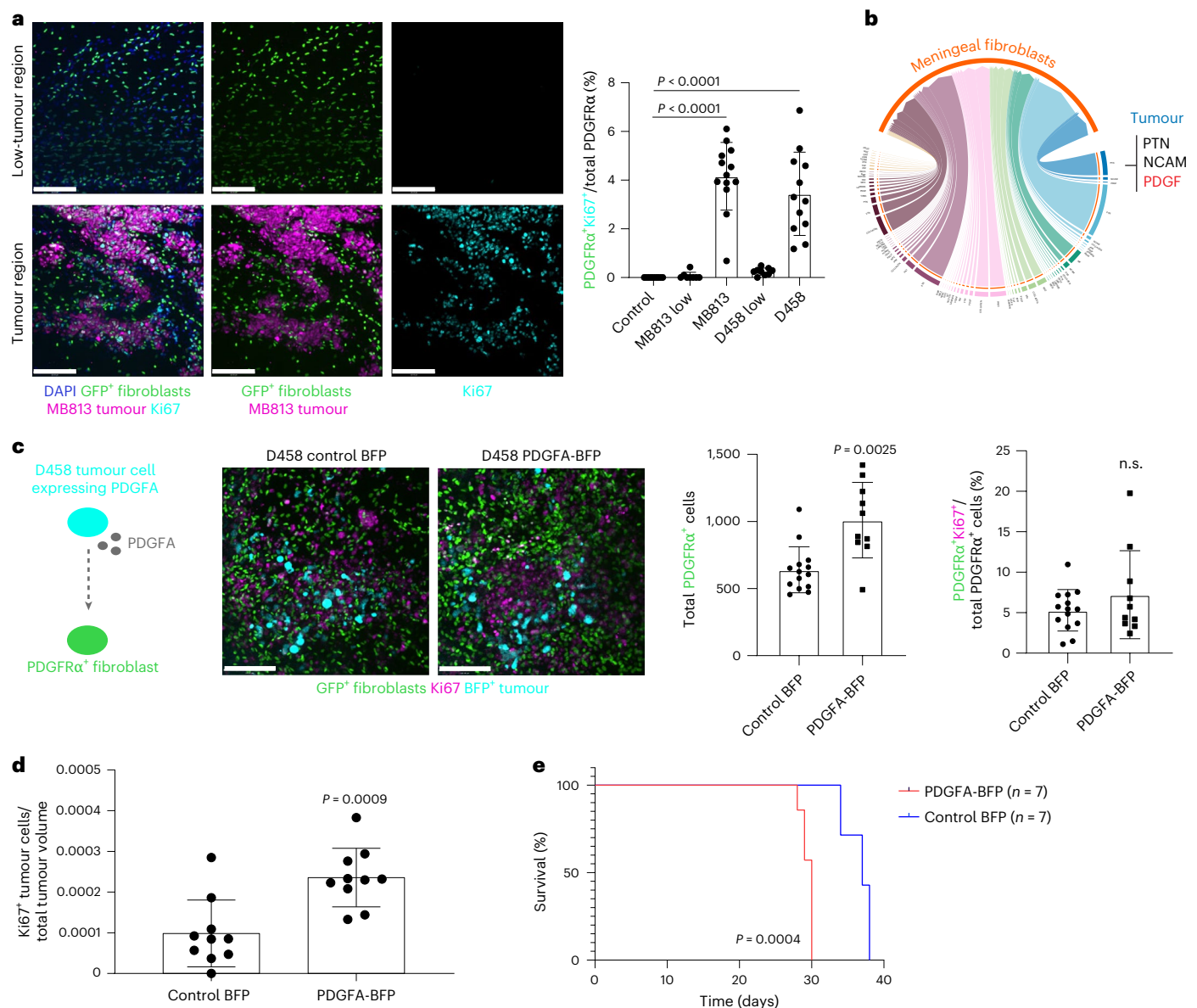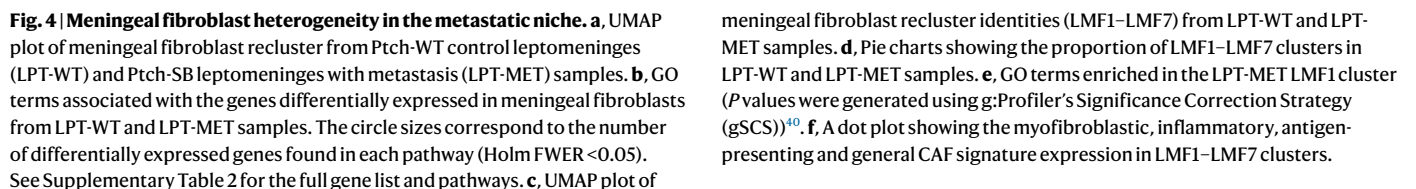
Fig. 3 | Meningeal fibroblasts are recruited and undergo proliferation in the presence of tumour cells. a, Whole-mount spinal leptomeninges from *Pdgfra-H2BeGFP*/NSG mice implanted with MB813−mCherry and D458−mCherry cells into the lateral ventricle and fluorescently labelled with GFP⁺ fibroblasts, mCherry (MB813 tumour), Ki67 and DAPI. The proportion of PDGFRα and Ki67 double-positive cells in control (sham injection) and MB813 and D458 (tumour low and high regions) samples was quantified per field of view ($n = 10, 8, 13, 9$ and 12 images for control, MB813 low, MB813, D458 low and D458, respectively). **b**, A chord diagram of scRNA-seq data highlighting the signalling pathways from Ptch-SB metastatic tumour cells to the meningeal fibroblasts. **c**, A schematic representation of the experimental design with D458 cells overexpressing PDGFA and signalling to PDGFRα⁺ meningeal fibroblasts (far left). Whole-mount spinal leptomeninges fluorescently labelled with GFP⁺ fibroblasts, BFP⁺ tumour and Ki67 from *Pdgfra-H2BeGFP*/NSG mice implanted with D458 cells expressing control BFP and PDGFA-BFP into the lateral ventricle. The total PDGFRα⁺ cells and proportion of PDGFRα and Ki67 double-positive cells were quantified per field of view ($n = 14$ and $n = 10$ images for control BFP and PDGFA-BFP, respectively). **d**, Quantifications from whole-mount spinal leptomeninges of NSG mice implanted with D458 GFP-Luc control-BFP and D458 GFP-Luc PDGFA-BFP into the lateral ventricle and fluorescently labelled with Ki67. The total number of Ki67⁺ GFP⁺ tumour cells was normalized to the total GFP⁺ tumour volume per field of view ($n = 10$ images per group). **e**, Kaplan−Meier survival analysis from NSG mice implanted with D458 GFP-Luc control-BFP ($n = 7$ mice) and D458 GFP-Luc PDGFA-BFP ($n = 7$ mice) into the lateral ventricle (log-rank (Mantel−Cox) test was performed). P values were generated from two-tailed unpaired t-test with Welch's correction, the centre line represents mean and the error bars represent the standard deviation for **a**, **c** and **d**. n.s., not significant ($P = 0.3166$). Scale bars, 120 µm (**a** and **c**).

from 1,601 healthy LPT-WT fibroblasts and 4,510 LPT-MET associated fibroblasts. We identified a subpopulation of LPT-MET fibroblasts that were transcriptionally distinct from LPT-WT fibroblasts (Fig. 4a). We performed differential gene expression and pathway analysis to identify any functional heterogeneity (Fig. 4b and Supplementary Table 2). Transcriptional programs specific to LPT-MET fibroblasts included TGFβ, BMP, WNT and ERK1/2 pathways (Fig. 4b and Extended Data Fig. 5a). LPT-MET fibroblasts differentially expressed genes associated

with ECM organization, leukocyte migration, angiogenesis, cell death, differentiation and proliferation (Extended Data Fig. 5b–d). Unsupervised clustering of meningeal fibroblast populations identified seven unique clusters of fibroblasts, which we have designated as LMF1 through LMF7 (Fig. 4c). Cluster LMF1 was associated with ECM remodelling genes, including *Mfap4*, *Fbln1*, *Bgn*, *Itih5* and *Vtn* (Extended Data Fig. 6a) and was significantly higher in LPT-MET compared with LPT-WT fibroblasts (Fig. 4d and Extended Data Fig. 6b). By contrast, cluster

Fig. 4 | Meningeal fibroblast heterogeneity in the metastatic niche. a, UMAP plot of meningeal fibroblast recluster from Ptch-WT control leptomeninges (LPT-WT) and Ptch-SB leptomeninges with metastasis (LPT-MET) samples. **b**, GO terms associated with the genes differentially expressed in meningeal fibroblasts from LPT-WT and LPT-MET samples. The circle sizes correspond to the number of differentially expressed genes found in each pathway (Holm FWER <0.05). See Supplementary Table 2 for the full gene list and pathways. **c**, UMAP plot of meningeal fibroblast recluster identities (LMF1–LMF7) from LPT-WT and LPT-MET samples. **d**, Pie charts showing the proportion of LMF1–LMF7 clusters in LPT-WT and LPT-MET samples. **e**, GO terms enriched in the LPT-MET LMF1 cluster (*P* values were generated using g:Profiler's Significance Correction Strategy (gSCS))[40]. **f**, A dot plot showing the myofibroblastic, inflammatory, antigen-presenting and general CAF signature expression in LMF1–LMF7 clusters.

LMF2 was higher in LPT-WT fibroblasts and marked by high expression of *Tgfbi*, *Gpc3* and *Trf* (Fig. 4d and Extended Data Fig. 6a,b). Cluster LMF5 displayed a tumour-like signature with increased expression of *Stmn1*, *Hmgb2* and *Sox11*, and cluster LMF7 expressed immunoregulatory genes, including *C1qa*, *C1qb*, *Lyz2*, *Cd74* and *Cxcl2* (Extended Data Fig. 6a).

We focused on cluster LMF1 because it is overrepresented in LPT-MET samples as compared with LPT-WT controls (Fig. 4d) and has

a transcriptional program associated with ECM organization, wound healing, cell adhesion and proliferation (Fig. 4e). LMF1-enriched transcriptional pathways closely resemble metastasis-associated pathways identified in Fig. 4b, consistent with LMF1-type meningeal fibroblasts being the dominant fibroblast population in the metastatic niche. Furthermore, as LPT-MET transcriptional programs resemble those of cancer-associated fibroblasts (CAF) from systemic (non-neural) tumours, we compared our LPT-MET fibroblast signatures with

published CAF signatures[28,29]. The LMF1 cluster most closely resembled myofibroblastic CAFs, characterized by *Col1a1*, *Col4a1*, *Tgfb1* expression and general CAFs, characterized by *Pdgfra* and *Pdgfrb* expression, whereas the LMF7 cluster resembled inflammatory, or antigen-presenting, CAF signatures (Fig. 4f). These findings are consistent with a model in which the presence of metastatic tumour cells recruit and reprogram meningeal fibroblasts.

CAFs progressively co-evolve with tumour cells over time as cancers progress[30]. To test the model of temporally evolving fibroblasts in our MB experimental system, we contrasted the meningeal fibroblasts between LPT-MET samples of low metastatic burden with higher metastatic burden (Extended Data Fig. 7a). Highly metastatic samples had a trend towards an increased representation of the LMF1 and LMF5 clusters as compared with LPT-MET samples with a lower metastatic burden (Extended Data Fig. 7b). Fibroblasts from low LPT-MET samples transcriptionally resembled inflammatory CAFs, while fibroblasts from high LPT-MET samples resembled myofibroblastic CAFs (Extended Data Fig. 7c). The differences between the transcriptional programs of the fibroblasts from low and high LPT-MET samples (Extended Data Fig. 7d and Supplementary Table 3) support a model in which the fibroblasts are progressively recruited and reprogrammed in the niche with the accumulation of metastatic tumour cells. Interference with the recruitment, reprogramming and/or intercellular signalling between tumour cells and meningeal fibroblasts in the metastatic niche could represent a strategy for the prevention of metastatic MB or the treatment of established metastases.

Fibroblast-derived BMP ligands enhance metastatic growth

To determine the specific molecular mechanisms by which meningeal fibroblasts support metastatic cells, we analysed the incoming tumour-specific CellChat data. Prominently, BMP signalling from the meningeal fibroblasts was enriched in LPT-MET samples (Extended Data Fig. 8a,b). Most of the major signalling pathway networks were between neuronal cell types, and there were only a few pathways, including BMP, HSPG, FGF, WNT and HH signalling, in which the 'sender' population was from the leptomeningeal microenvironment (Extended Data Fig. 8b). In control LPT-WT samples, *Bmp5* was expressed by the meningeal fibroblasts and signalled to pericytes (Fig. 5a,d). With low metastatic burden, meningeal fibroblasts expressed *Bmp4*, *Bmp5* and *Bmp7* to signal to the metastatic tumour cells and local astrocytes, ependyma, smooth muscle cells and pericytes (Fig. 5b,d). Upon progression to high metastatic burden, meningeal fibroblasts express *Bmp4* and *Bmp7* to act on the tumour cells (Fig. 5c,d). We confirmed that BMP4 and BMP7 protein was detected in the LPT-MET niche, but not primary tumours, using immunofluorescence (IF) (Fig. 5e,f). BMP4 and BMP7 signals preferentially associated with the GFP-labelled LPT-MET cells, as compared with the GFP-negative microenvironment cells (Fig. 5e and Fig. 5f, respectively). BMP signalling activity can be measured by phosphorylation of SMAD1 and SMAD5 (pSMAD1/5)[31]. Indeed,

LPT-MET cells exhibited elevated levels of pSMAD1/5 not observed in primary tumour controls (Fig. 5g). Furthermore, BMP target genes, *Id1* and *Id2* (ref. 32), were transcriptionally upregulated in LPT-MET tumour cells, as compared with primary tumour cells (Fig. 5h). In an orthogonal model, sonic hedgehog (SHH) MBs from Smoothened A1 genetically engineered mice also exhibited increased expression of BMP4, BMP7 and pSMAD1/5 in the LPT-MET samples as compared with the primary tumour (Extended Data Fig. 9a–c)[33].

As ID1 is a BMP target gene, we compared single-cell transcriptomes of *Id1*-positive versus *Id1*-negative LPT-MET tumour cells to identify BMP-associated transcriptional programs, which showed elevated transcription of cell cycle progression genes in the *Id1*-positive cells (Fig. 6a). Consistently, approximately 27% of ID1-positive cells expressed the proliferation marker Ki67 (Fig. 6b). We conclude that reprogrammed fibroblasts secrete BMP4 and BMP7 in the metastatic niche, enhancing the BMP signalling and proliferation of LPT-MET cells.

To formally test a causative role for fibroblast-derived BMP signalling in LPT-MET cells, we overexpressed a constitutively active (CA) BMPR1A (Q233D) in D458 MB tumour cells expressing luciferase and ZsGreen (Luc-ZsGreen)[34]. BMPR1A-CA-expressing tumour cells and vector control cells were implanted into the lateral ventricle of immunocompromised (NOD.Cg-Prkdc scid Il2rg tm1Wjl/SzJ; NSG) mice to assess leptomeningeal colonization. BMPR1A-CA-expressing tumour cells, but not vector control cells, exhibited enhanced leptomeningeal colonization, with a greater proportion of mice displaying spinal colonization (3/5 mice), as compared with control tumour cells (0/5 control mice; Fig. 6c,d). We also quantified the GFP-positive area along the craniospinal axis as a measure of tumour burden after the humane endpoint and demonstrated increased tumour burden in mice engrafted with BMPR1A-CA-expressing cells (Fig. 6e). Furthermore, mice engrafted with BMPR1A-CA-expressing cells displayed worse overall survival compared with control mice (Fig. 6f). These findings are consistent with BMP signalling from recruited and reprogrammed fibroblasts promoting the growth of established leptomeningeal metastases.

Metastasis-associated fibroblasts support tumour colonization

To further investigate the function of reprogrammed fibroblasts in the metastatic cascade, we performed in vivo co-implantation studies using group 3 MB patient-derived xenografts. The MB411 line was transduced with GFP and luciferase (GFP-Luc) and implanted into the cerebellum of NSG mice. At the humane endpoint, the primary tumour and spinal leptomeninges with metastasis were collected, and a single-cell suspension was generated for fluorescence-activated cell sorting (FACS). To isolate the PDGFRα-positive fibroblasts from the metastatic leptomeninges (MB-MAFs), we followed a gating strategy that excluded the GFP-labelled tumour cells, pericytes/smooth muscle cells (marked by CD146), immune cells (CD45) and endothelial cells


Fig. 5 | Meningeal fibroblast-derived BMP ligands signal to metastatic tumour cells. a–c, Chord diagram (top) and schematic diagram (bottom) demonstrating the BMP signalling interactions from meningeal fibroblasts to the microenvironment of non-tumour leptomeninges (LPT-WT) (**a**), low leptomeningeal metastatic burden (low LPT-MET) (**b**) and high leptomeningeal metastatic burden (high LPT-MET) samples (**c**), with BMPR1A_R2 denoted as 1A_R2 and BMPR1B_R2 denoted as 1B_R2. **d**, Violin plots showing *Bmp5*, *Bmp4* and *Bmp7* expression in meningeal fibroblasts from LPT-WT, low LPT-MET and high LPT-MET scRNA-seq samples. **e,f**, Ptch-SB spinal cord with metastasis (LPT-MET) and primary tumour cross-sections fluorescently labelled with GFP, ERTR7, DAPI and BMP4 (**e**) or BMP7 (**f**). The proportion of tumour cells (GFP⁺) and microenvironment cells (GFP⁻DAPI⁺) close to BMP4-positive signal (*n* = 14 and *n* = 15 images for LPT-MET and primary, respectively) (**e**) and BMP7-positive signal (*n* = 13 and *n* = 8 images for LPT-MET and primary, respectively) (**f**) was

quantified per field of view. **g**, Ptch-SB spinal cord LPT-MET and primary tumour cross-sections fluorescently labelled with GFP, pSMAD1/5 and ERTR7. The pSMAD and GFP double-positive cells normalized to total GFP volume were quantified in LPT-MET samples and primary tumour core and boundary regions per field of view (*n* = 37, 10 and 9 images for LPT-MET, core and boundary, respectively). *P* values were generated using two-tailed unpaired *t*-test with Welch's correction, the centre line represents the mean and error bars represent the standard deviation, **P* < 0.0001. Scale bars, 120 μm (**e–g**). **h**, Box plots showing *Id1* and *Id2* mean expression per sample in primary tumour (*n* = 4 mice) and LPT-MET tumour cells (*n* = 4 mice) from the scRNA-seq data. The centre line represents the median (50% percentile), the hinges represent 25% and 75% percentiles, and the whiskers represent the 1.5 interquartile range. *P* values were generated using a two-tailed Student's *t*-test.

(CD31) (Fig. 7a). We also sorted the GFP-positive MB411 primary tumour cells for co-implantation with the isolated PDGFRα-positive fibroblasts (designated as MB411 + MB-MAFs) into the lateral ventricles of NSG mice (Fig. 7b,c). Eight weeks after implantation, the bioluminescence signal along the craniospinal axis was higher in the mice co-implanted with

MB411 + MB-MAFs, as compared with mice implanted with MB411 cells alone (Fig. 7d). Furthermore, mice co-implanted with MB411 + MB-MAFs developed spinal colonization more frequently (4/5 mice) than mice implanted with MB411 cells alone (1/5 mice; Fig. 7d). Quantification of the GFP-positive area along the craniospinal axis demonstrated that
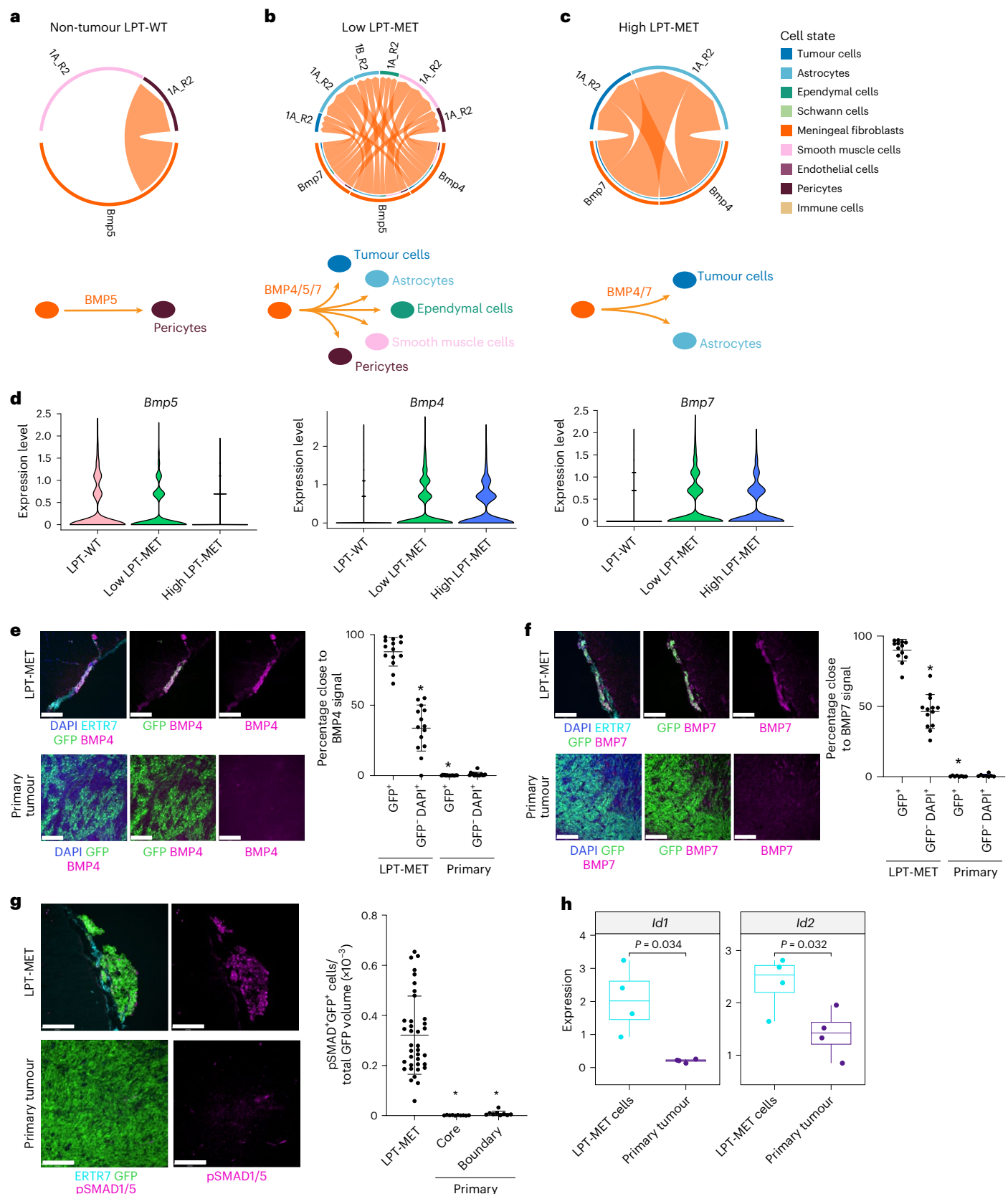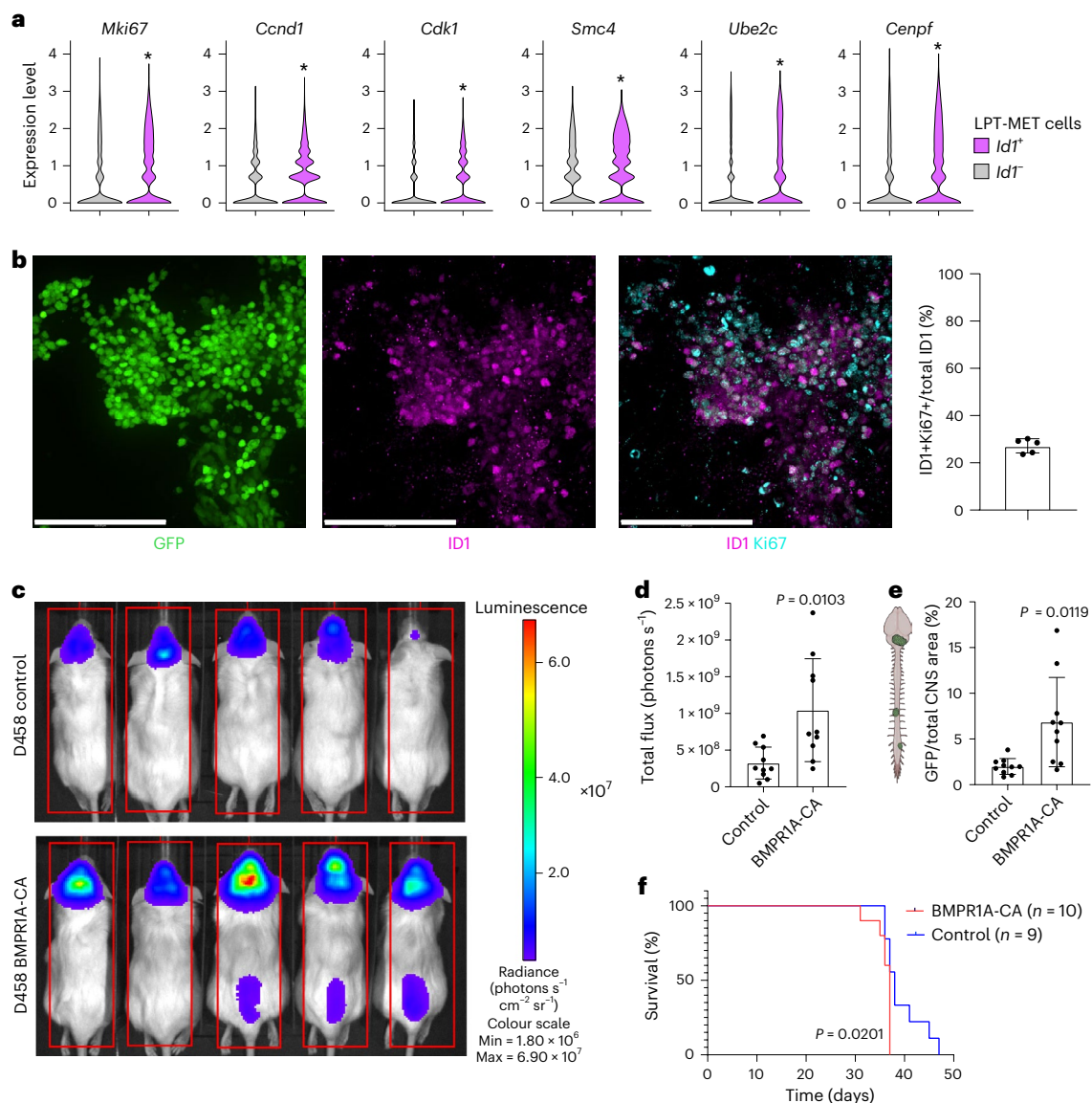
Fig. 6 | Enhanced cell cycle progression and leptomeningeal colonization in metastatic tumour cells with active BMP signalling. a, Violin plots showing cell cycle progression gene expression in *Id1⁻* and *Id1⁺* LPT-MET tumour cells from the scRNA-seq data. Two-tailed Student's *t*-test was performed. *$P < 2.22 \times 10^{-16}$. **b,** Whole-mount Ptch-SB spinal leptomeninges with metastasis fluorescently labelled with GFP, ID1 and Ki67 with the proportion of ID1 and Ki67 double-positive cells quantified per field of view (*n* = 5 images; the centre line represents the mean, and error bars represent the standard deviation; scale bars, 120 μm). **c,** BLI 38 days after NSG mice were implanted with D458 Luc-ZsGreen tumour cells expressing control and BMPR1A-CA into the lateral ventricle (cohort of *n* = 5 mice per group are shown). **d,** Total flux (photons s⁻¹) quantifications of D458 Luc-ZsGreen control and BMPR1A-CA (*n* = 10 mice per group). **e,** The proportion of GFP-positive area on the surface of the brain, spinal cord and peripheral nerves of D458 Luc-ZsGreen control and BMPR1A-CA (*n* = 10 mice per group). *P* values were generated using two-tailed unpaired *t*-test with Welch's correction, the centre line represents the mean, and error bars represent the standard deviation for **d** and **e**. **f,** Kaplan–Meier survival analysis from NSG mice implanted with D458 Luc-ZsGreen control (*n* = 9 mice) and BMPR1A-CA (*n* = 10 mice) into the lateral ventricle (log-rank (Mantel–Cox) test was performed).

the addition of MB-MAFs massively increased the tumour burden as compared with controls (Fig. 7e,f). This observed increase in tumour burden led to worse overall survival in mice co-implanted with MB-MAFs compared with control mice (Fig. 7g). We conclude that reprogrammed MB-MAFs play an active causal role in the establishment of leptomeningeal metastases.

To target MB-MAF function, we treated xenografted mice with a PDGFRα neutralizing antibody. The D458 Luc-ZsGreen tumour cells were implanted into the lateral ventricle of NSG mice. Ten days after implantation, IgG control and anti-PDGFRα neutralizing antibody was administered into the lateral ventricles of xenografted mice and the mice were monitored until the humane endpoint (Fig. 7h). After anti-PDGFRα treatment, there was a reduced proportion of mice with

spinal colonization (2/5 mice) compared with mice treated with the IgG control (4/5 mice; Fig. 7i), leading to prolonged survival (Fig. 7j). Thus, metastasis-associated fibroblasts support leptomeningeal colonization, and inhibiting fibroblast function improves overall survival in patient-derived xenograft models.

Together, our findings support a model in which meningeal fibroblasts are recruited in the presence of metastasis, partly through PDGFA secretion. Meningeal fibroblast recruitment is followed by proliferation and reprogramming to become MB-MAFs, which subsequently secrete BMP4/7, driving tumour cell division and enhancing leptomeningeal colonization. In turn, the MB-MAFs in a 'folie a deux' support additional leptomeningeal colonization and growth of existing metastases (Extended Data Fig. 10).
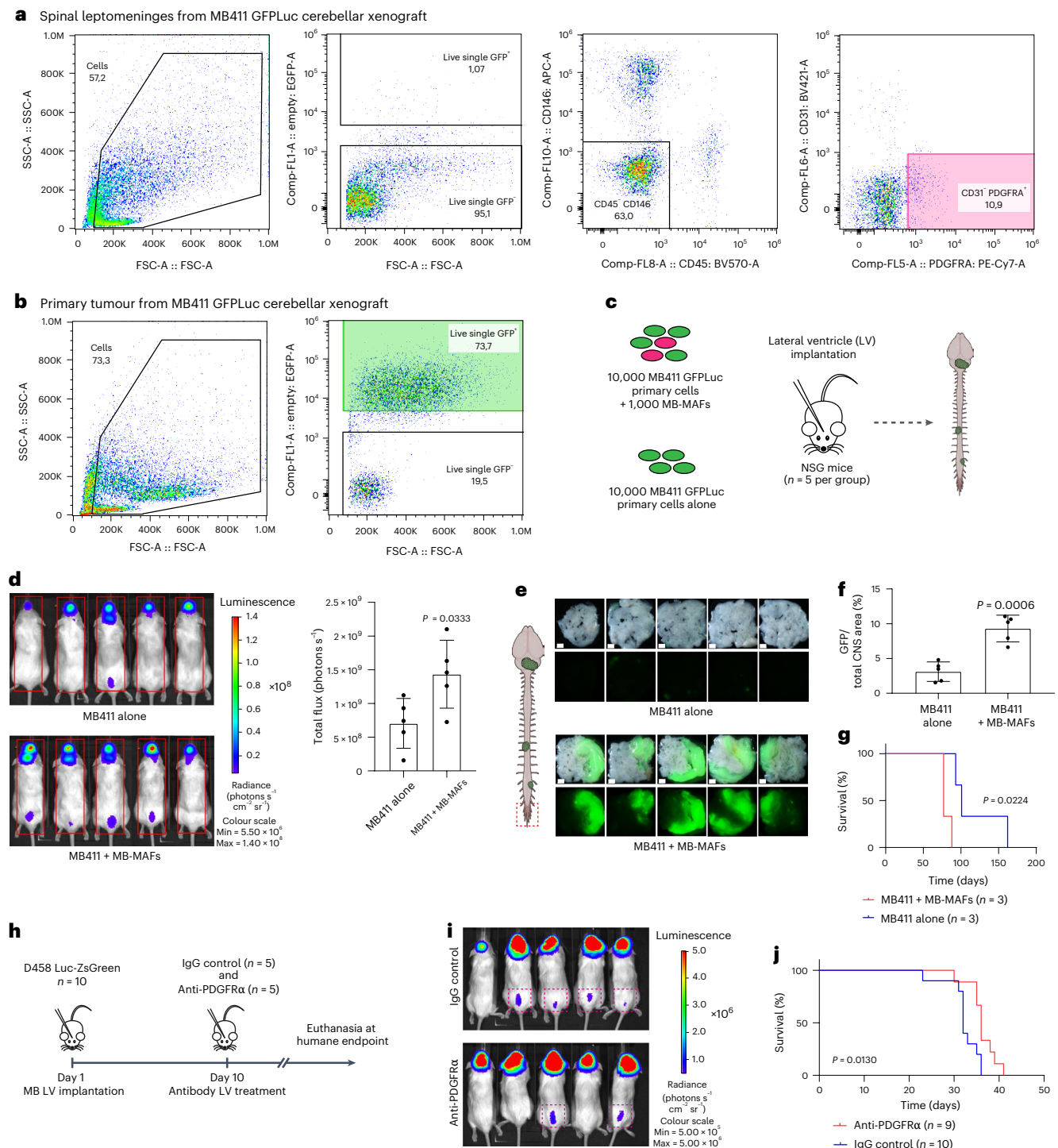
Fig. 7 | Metastasis-associated fibroblasts support leptomeningeal colonization. a,b, FACS plots demonstrating the gating strategy used to sort live GFP⁻/CD45⁻/CD146⁻/CD31⁻/PDGFRA⁺ fibroblasts from the spinal leptomeninges (**a**) and live GFP⁺ tumour cells from the primary tumour of NSG mice with cerebellar implantation of MB411 GFPLuc (**b**). The proportions of cells within the indicated gates are shown. See also Supplementary Data 1 for the full gating strategy. **c,** A schematic representation of the co-implantation experiments into the leptomeninges of NSG mice. **d,** BLI and total flux (photons s⁻¹) quantifications 8 weeks after NSG mice were implanted with MB411 GFPLuc and MB411 GFPLuc co-implanted with metastasis-associated fibroblasts (MB411 + MB-MAFs) isolated by FACS (*n* = 5 mice per group). **e,** Stereomicroscope images of dissected peripheral nerves (highlighted in schematic with dashed red box) from NSG mice implanted with MB411 alone and MB411 + MB-MAFs (scale bars, 1 mm). **f,** The proportion of GFP-positive area on the surface of the brain,

spinal cord and peripheral nerves of NSG mice implanted with MB411 alone and MB411 + MB-MAFs into the lateral ventricle (*n* = 5 mice per group). *P* values were generated using two-tailed unpaired *t*-test with Welch's correction; the centre line represents the mean, and error bars represent the standard deviation for **d** and **f**. **g,** Kaplan–Meier survival analysis from NSG mice implanted with MB411 alone and MB411 + MB-MAFs into the lateral ventricle (*n* = 3 mice per group). **h,** A schematic representation of the anti-PDGFRα treatment experiments. **i,** BLI 19 days after treatment of NSG mice implanted with D458 Luc-ZsGreen into the lateral ventricle with either IgG control or anti-PDGFRα neutralizing antibody administered into the lateral ventricle (cohort of *n* = 5 mice per group are shown). The dashed magenta box highlights spinal colonization. **j,** Kaplan–Meier survival analysis from NSG mice implanted with D458 Luc-ZsGreen and treated with either IgG control (*n* = 10 mice) or anti-PDGFRα neutralizing antibody (*n* = 9 mice). *P* values were generated using log-rank (Mantel–Cox) test for survival analyses in **g** and **j**.

Discussion

The vast majority of MB deaths are secondary to metastatic recurrent disease. Despite the known published marked differences between metastatic and primary MB[13], further supported by our findings, most MB research continues to be focused on primary tumours. This is similar to most systemic cancers due to limitations of reliable models and patient tissues, as there are only very few clinical scenarios in which it is advantageous to patients to surgically remove metastases. Our data support the critical importance of studying the metastatic tumours if we hope to develop therapies for metastasis.

Here, we demonstrate that the TME in the leptomeninges is complex, with involvement of multiple cell types in a symbiotic local ecosystem. While the current studies are focused on the meningeal fibroblasts, we hypothesize that further analysis of our datasets will reveal additional intercellular signalling events between the LPT-MET cells and other cell types of the leptomeningeal niche. The complexity of the niche and, indeed, the experiments in the current studies suggest that targeting the metastatic niche could influence or even abrogate the growth of LPT-MET cells in the leptomeninges. In parallel to the multistep process of systemic metastases, establishment of the leptomeningeal metastatic niche appears to be a multistep process: from local recruitment of meningeal fibroblasts to replication and reprogramming of meningeal fibroblasts towards a MB-MAF fate, followed by MB-MAF secretion of BMPs acting on the LPT-MET cells and induction of LPT-MET proliferation to further produce and secrete additional pro-tumourigenic signals.

The PDGF–BMP axis we have observed in model systems of leptomeningeal metastases should ideally be rigorously confirmed in surgical biopsy samples of human leptomeningeal MB. However, as there is little or no clinical benefit, and great morbidity from removal of laminar leptomeningeal metastases, these specimens are exceptionally rare and not currently available. Furthermore, while the current study focuses on group 3 and SHH MB, the extent to which the PDGF–BMP axis identified varies across metastases from the four MB subgroups cannot currently be determined. Indeed, additional work comparing metastases from MBs of different subgroups is desperately needed to advance the field.

Many patients with MB appear disease-free after receiving modern therapies as measured by magnetic resonance imaging of the brain and spinal cord[35–37]. However, metastatic recurrence in the leptomeninges, which becomes apparent on magnetic resonance imaging at relapse, after prior imaging had demonstrated no evidence of disease, is the most common cause of mortality[38,39]. Targeting the metastatic niche may require different strategies based on the particular step or process of the metastatic cascade. We hypothesize that therapies that prevent metastatic colonization will be more effective than attempts to treat established leptomeningeal metastases.

The high complexity of the heterogeneous leptomeningeal metastatic niche could be an Achilles' heel, offering multiple targets for combinatorial therapy. Anti-niche strategies could be aimed against specific molecular signalling pathways or against specific TME cell types. We showed that a single intrathecal dose of anti-PDGFRα antibodies diminished leptomeningeal disease in our in vivo models. We propose that clinical trial(s) of anti-PDGFRα antibodies in humans could be undertaken to test its efficacy in either prevention of metastases after standard therapy, or for the treatment of established metastatic disease at recurrence. The lack of highly recurrent somatic mutations that could serve as rational drug targets across MB subgroups has prevented the development of small molecule targeted therapy for patients with MB. As there is no genomic instability in the cells of the metastatic TME, there may be fewer opportunities for the evolution of therapy resistance. Future studies of the leptomeningeal metastatic niche will enable opportunities to develop therapies that prevent or treat metastatic MB through niche inhibition.

Online content

Any methods, additional references, Nature Portfolio reporting summaries, source data, extended data, supplementary information, acknowledgements, peer review information; details of author contributions and competing interests; and statements of data and code availability are available at https://doi.org/10.1038/s41556-025-01660-7.

References

1. Gibson, P. et al. Subtypes of medulloblastoma have distinct developmental origins. *Nature* **468**, 1095–1099 (2010).
2. Vladoiu, M. C. et al. Childhood cerebellar tumours mirror conserved fetal transcriptional programs. *Nature* **572**, 67–73 (2019).
3. Hovestadt, V. et al. Resolving medulloblastoma cellular architecture by single-cell genomics. *Nature* **572**, 74–79 (2019).
4. Hendrikse, L. D. et al. Failure of human rhombic lip differentiation underlies medulloblastoma formation. *Nature* **609**, 1021–1028 (2022).
5. Smith, K. S. et al. Unified rhombic lip origins of group 3 and group 4 medulloblastoma. *Nature* **609**, 1012–1020 (2022).
6. Ramaswamy, V. & Taylor, M. D. Medulloblastoma: from myth to molecular. *J. Clin. Oncol.* **35**, 2355–2363 (2017).
7. Juraschka, K. & Taylor, M. D. Medulloblastoma in the age of molecular subgroups: a review. *J. Neurosurg. Pediatr.* **24**, 353–363 (2019).
8. Zeltzer, P. M. et al. Metastasis stage, adjuvant treatment, and residual tumor are prognostic factors for medulloblastoma in children: conclusions from the Children's Cancer Group 921 randomized phase III study. *J. Clin. Oncol.* **17**, 832–845 (1999).
9. Mulhern, R. K. et al. Neurocognitive deficits in medulloblastoma survivors and white matter loss. *Ann. Neurol.* **46**, 834–841 (1999).
10. Coltin, H. et al. The burden of surviving childhood medulloblastoma: a population-based, matched cohort study in Ontario, Canada. *J. Clin. Oncol.* **41**, 2372–2381 (2023).
11. Van Ommeren, R., Garzia, L., Holgado, B. L., Ramaswamy, V. & Taylor, M. D. The molecular biology of medulloblastoma metastasis. *Brain Pathol.* **30**, 691–702 (2020).
12. Fults, D. W., Taylor, M. D. & Garzia, L. Leptomeningeal dissemination: a sinister pattern of medulloblastoma growth. *J. Neurosurg. Pediatr.* https://doi.org/10.3171/2018.11.PEDS18506 (2019).
13. Wu, X. et al. Clonal selection drives genetic divergence of metastatic medulloblastoma. *Nature* **482**, 529–533 (2012).
14. Morrissy, A. S. et al. Divergent clonal selection dominates medulloblastoma at recurrence. *Nature* **529**, 351–357 (2016).
15. Chang, C. H., Housepian, E. M. & Herbert, C. Jr. An operative staging system and a megavoltage radiotherapeutic technic for cerebellar medulloblastomas. *Radiology* **93**, 1351–1359 (1969).
16. Garzia, L. et al. A hematogenous route for medulloblastoma leptomeningeal metastases. *Cell* **172**, 1050–1062 (2018).
17. Lascelles, P. T. Cerebrospinal fluid in diseases of the nervous system. *J. Clin. Pathol.* **34**, 453 (1981).
18. Chi, Y. et al. Cancer cells deploy lipocalin-2 to collect limiting iron in leptomeningeal metastasis. *Science* **369**, 276–282 (2020).
19. Boire, A. et al. Complement component 3 adapts the cerebrospinal fluid for leptomeningeal metastasis. *Cell* **168**, 1101–1113 e13 (2017).
20. Goodrich, L. V., Milenkovic, L., Higgins, K. M. & Scott, M. P. Altered neural cell fates and medulloblastoma in mouse patched mutants. *Science* **277**, 1109–1113 (1997).
21. Mastorakos, P. & McGavern, D. The anatomy and immunology of vasculature in the central nervous system. *Sci. Immunol.* **4**, eaav0492 (2019).
22. Dorrier, C. E., Jones, H. E., Pintarić, L., Siegenthaler, J. A. & Daneman, R. Emerging roles for CNS fibroblasts in health, injury and disease. *Nat. Rev. Neurosci.* **23**, 23–34 (2022).

23. Vanlandewijck, M. et al. A molecular atlas of cell types and zonation in the brain vasculature. *Nature* https://doi.org/10.1038/nature25739 (2018).

24. Saunders, A. et al. Molecular diversity and specializations among the cells of the adult mouse brain. *Cell* **174**, 1015–1030 (2018).

25. Jin, S. et al. Inference and analysis of cell-cell communication using CellChat. *Nat. Commun.* **12**, 1088 (2021).

26. Pietilä, R. et al. Molecular anatomy of adult mouse leptomeninges. *Neuron* **111**, 3745–3764 (2023).

27. Hamilton, T. G., Klinghoffer, R. A., Corrin, P. D. & Soriano, P. Evolutionary divergence of platelet-derived growth factor alpha receptor signaling mechanisms. *Mol. Cell. Biol.* https://doi.org/10.1128/mcb.23.11.4013-4025.2003 (2003).

28. Luo, H. et al. Pan-cancer single-cell analysis reveals the heterogeneity and plasticity of cancer-associated fibroblasts in the tumor microenvironment. *Nat. Commun.* **13**, 6619 (2022).

29. Lavie, D., Ben-Shmuel, A., Erez, N. & Scherz-Shouval, R. Cancer-associated fibroblasts in the single-cell era. *Nat. Cancer* **3**, 793–807 (2022).

30. D'Arcangelo, E., Wu, N. C., Cadavid, J. L. & McGuigan, A. P. The life cycle of cancer-associated fibroblasts within the tumour stroma and its importance in disease outcome. *Br. J. Cancer* **122**, 931–942 (2020).

31. Kretzschmar, M., Liu, F., Hata, A., Doody, J. & Massagué, J. The TGF-beta family mediator Smad1 is phosphorylated directly and activated functionally by the BMP receptor kinase. *Genes Dev.* **11**, 984–995 (1997).

32. Hollnagel, A., Oehlmann, V., Heymer, J., Rüther, U. & Nordheim, A. Id genes are direct targets of bone morphogenetic protein induction in embryonic stem cells. *J. Biol. Chem.* **274**, 19838–19845 (1999).

33. Hallahan, A. R. et al. The SmoA1 mouse model reveals that notch signaling is critical for the growth and survival of sonic hedgehog-induced medulloblastomas. *Cancer Res.* **64**, 7794–7800 (2004).

34. Zou, H., Wieser, R., Massagué, J. & Niswander, L. Distinct roles of type I bone morphogenetic protein receptors in the formation and differentiation of cartilage. *Genes Dev.* **11**, 2191–2203 (1997).

35. Packer, R. J. et al. Phase III study of craniospinal radiation therapy followed by adjuvant chemotherapy for newly diagnosed average-risk medulloblastoma. *J. Clin. Oncol.* **24**, 4202–4208 (2006).

36. Lannering, B. et al. Hyperfractionated versus conventional radiotherapy followed by chemotherapy in standard-risk medulloblastoma: results from the randomized multicenter HIT-SIOP PNET 4 trial. *J. Clin. Oncol.* **30**, 3187–3193 (2012).

37. Gajjar, A. et al. Risk-adapted craniospinal radiotherapy followed by high-dose chemotherapy and stem-cell rescue in children with newly diagnosed medulloblastoma (St Jude Medulloblastoma-96): long-term results from a prospective, multicentre trial. *Lancet Oncol.* **7**, 813–820 (2006).

38. Sabel, M. et al. Relapse patterns and outcome after relapse in standard risk medulloblastoma: a report from the HIT-SIOP-PNET4 study. *J. Neurooncol.* **129**, 515–524 (2016).

39. Johnston, D. L. et al. Survival following tumor recurrence in children with medulloblastoma. *J. Pediatr. Hematol. Oncol.* **40**, e159–e163 (2018).

40. Reimand, J., Kull, M., Peterson, H., Hansen, J. & Vilo, J. g:Profiler—a web-based toolset for functional profiling of gene lists from large-scale experiments. *Nucleic Acids Res.* **35**, W193–W200 (2007).

Namal Abeysundara[1,2,19], **Alexandra Rasnitsyn**[1,2,3,19], **Vernon Fong** [1,2,4,19], **Alexander Bahcheli** [5,6], **Randy Van Ommeren**[1,2,4], **Kyle Juraschka**[1,2,4], **Maria Vladoiu**[1,2,4], **Winnie Ong**[1,2,4], **Bryn Livingston**[1,2,4], **Pasqualino de Antonellis** [1,2], **Michelle Ly**[1,2,4], **Borja López Holgado**[1,2], **Olga Sirbu** [1,2,3], **Shahrzad Bahrampour** [1,2], **Hyun-Kee Min**[1,2,6], **Jerry Fan**[1,2,6], **Carolina Nor**[1,2], **Abhirami Visvanathan**[1,2], **Jiao Zhang** [1,2,7,8], **Hao Wang**[1,2], **Lei Qin**[1,2], **Ning Huang**[1,2], **Jonelle Pallotta**[1,2], **Tajana Douglas**[1,2], **Esta Mak**[1,2], **Haipeng Su**[1,2], **Karen Ng** [9], **Kevin Yang Zhang** [10], **Craig Daniels**[1,2,7,8], **Calixto-Hope G. Lucas** [10], **Charles G. Eberhart**[10], **Hailong Liu**[11], **Tao Jiang** [12], **Faiyaz Notta**[3,6,9], **Vijay Ramaswamy** [1,2,3], **Jüri Reimand** [3,5,6], **Marco Gallo** [7,8], **Jeremy N. Rich** [13,14], **Xiaochong Wu**[1,2,7,8], **Xi Huang** [1,2,6] & **Michael D. Taylor** [1,2,3,4,7,8,15,16,17,18] ✉

[1]Developmental and Stem Cell Biology Program, The Hospital for Sick Children, Toronto, Ontario, Canada. [2]The Arthur and Sonia Labatt Brain Tumour Research Centre, The Hospital for Sick Children, Toronto, Ontario, Canada. [3]Department of Medical Biophysics, University of Toronto, Toronto, Ontario, Canada. [4]Department of Laboratory Medicine and Pathobiology, University of Toronto, Toronto, Ontario, Canada. [5]Computational Biology Program, Ontario Institute for Cancer Research, Toronto, Ontario, Canada. [6]Department of Molecular Genetics, University of Toronto, Toronto, Ontario, Canada. [7]Texas Children's Cancer and Hematology Center, Houston, TX, USA. [8]Department of Pediatrics – Hematology/Oncology, Baylor College of Medicine, Houston, TX, USA. [9]PanCuRx Translational Research Initiative, Ontario Institute for Cancer Research, Toronto, Ontario, Canada. [10]Department of Pathology, Johns Hopkins School of Medicine, Baltimore, MD, USA. [11]Department of Radiotherapy, Beijing Tiantan Hospital, Capital Medical University, Beijing, China. [12]Department of Neurosurgery, Beijing Tiantan Hospital, Capital Medical University, Beijing, China. [13]Lineberger Comprehensive Cancer Center, University of North Carolina, Chapel Hill, NC, USA. [14]Department of Neurology, University of North Carolina, Chapel Hill, NC, USA. [15]Department of Surgery, University of Toronto, Toronto, Ontario, Canada. [16]Department of Neurosurgery, Baylor College of Medicine, Houston, TX, USA. [17]Department of Neurosurgery, Texas Children's Hospital, Houston, TX, USA. [18]Dan L Duncan Comprehensive Cancer Center, Baylor College of Medicine, Houston, TX, USA. [19]These authors contributed equally: Namal Abeysundara, Alexandra Rasnitsyn, Vernon Fong. ✉e-mail: mdt.cns@gmail.com

Methods

Research ethics board
This study obtained full ethics approval from the Hospital for Sick Children (research ethics board 0020020238 and 1000055059). All animal breeding and procedures were reviewed and approved by The Centre for Phenogenomics' (TCP) Animal Care Committee (Animal Use Protocols 25-0100H and 26-0151H). TCP is certified by the Canadian Council on Animal Care under the Animals for Research Act of Ontario.

Animal experiments
Mouse lines. *Ptch1*^{+/−}/*Math1-SB11*/*SB76*/*Math1-GFP* (active SB) mice with primary brain tumours and spinal metastases and *Ptch1*^{+/+}/*SB76*/*Math1-GFP* (inactive SB) non-tumour-bearing, age-matched (12–28 weeks) control mice were processed for scRNA-seq[13]. *T2Onc2*/*Nestin-SB100* (ref. [41]) mice were crossed with *Math1-GFP*/*SmoA1* (ref. [33]) to generate the transgenic mouse line SmoA1/Nestin-SB100/T2Onc2/Math1-GFP with high MB penetrance and metastatic burden. MB cerebellar and leptomeningeal implantation experiments were performed using randomized NOD.Cg-Prkdc scid Il2rg tm1Wjl/SzJ (NSG or NOD *scid* gamma; JAX stock #005557) mice at 4–10 weeks of age. *Pdgfra-H2BeGFP* (JAX stock #007669) mice were analysed individually (12–24 weeks of age) and backcrossed into the NSG background for six generations for patient-derived xenograft experiments (4–10 weeks of age). Both male and female mice were used in this study. All mice were euthanized at the humane endpoint when displaying symptoms of domed head, coat irregularities, decreased feeding, paresis, paralysis or circling movements. Veterinary staff and designated animal technicians at TCP were blinded to cohort assignments and monitored for the humane endpoint.

Mouse housing and husbandry. All mice were housed at TCP and housing room conditions were maintained as follows: 12-h light and 12-h dark cycles (lights on at 7:00; lights off at 19:00); room temperatures at 21–23 °C; humidity levels between 40% and 60%. All mice received extruded food pellets (Inotiv cat. no. TD.2918X) and reversed osmosis water (acidified and ultraviolet light filtration) via Avidity Science recirculating system and sterile quick disconnect water valves. Cages were changed every 2 weeks (cage bottom with new bedding; wire bar hopper and filter lid). Nesting material and enrichment devices were transferred to the new cage and changed only when soiled or damaged.

Cerebellar and leptomeningeal implantation experiments. Patient-derived xenograft lines were implanted into NSG mice or *Pdgfra-H2BeGFP*/NSG using a stereotaxic apparatus to stabilize the skull, and the following coordinates were used: for cerebellar implantation, from Lambda, *Y* (anterior–posterior): −2 mm, *X* (medial–lateral): 1 mm, *Z* (dorsal–ventral): −2 mm); and for leptomeningeal/lateral ventricle implantation, from Bregma, *Y* (anterior–posterior): −0.5 mm, *X* (medial–lateral): 1 mm, *Z* (dorsal–ventral): −2.5 mm). The following lines were used for implantation: D458 Luc-ZsGreen, D458 PDGFA-BFP, D458 control BFP, D458 GFP-Luc PDGFA-BFP, D458 GFP-Luc control BFP, D458 Luc-ZsGreen control BFP, D458 Luc-ZsGreen BMPR1A-CA, D458 mCherry, MB813 mCherry and MB411 GFP-Luc. Either 10,000 D458 cells, 50,000 MB411 cells or 200,000 MB813 cells in 3–4 µl of Neurobasal medium (ThermoFisher cat. no. 21103049) were implanted per mouse. For MB-MAF co-implantation studies, 50,000 MB411 GFP-Luc cells were implanted into the cerebellum of NSG mice. At the humane endpoint (approximately 2 months after implantation), the spinal meninges and primary tumour of xenografted mice were collected and dissociated into a single-cell suspension for antibody staining and FACS (see 'Fluorescence-activated cell sorting' section). Spinal meningeal samples were confirmed to be GFP-positive, indicating the presence metastatic tumour cells. Live GFP⁺ primary tumour cells and PDGFRA⁺ (GFP⁻/CD146⁻/CD45⁻/CD31⁻) meningeal fibroblasts (associated with metastasis; MB-MAFs) were sorted into separate Eppendorf

tubes containing Neurobasal medium. Samples were spun down at 300*g*, and pellets were resuspended in the appropriate volume of medium for implantation (10,000 primary tumour cells per 1.5 µl and 1,000 MB-MAFs per 1.5 µl). Resuspended primary tumour samples were mixed with either MB-MAFs or medium alone at a ratio of 10,000 primary tumour cells:1,000 MB-MAFs in 3 µl for implantation into the lateral ventricles of randomized, age-matched NSG mice. These processing steps for FACS and co-implantation experiments were all performed on the same day to ensure maximum cell viability.

Bioluminescence imaging. Xenografted mice subjected to bioluminescence imaging (BLI) were anaesthetized with 4% isoflurane in an induction chamber and given intraperitoneal injections of 150 mg kg⁻¹ of IVISBrite D-luciferin (PerkinElmer cat. no. 122799). Five minutes after intraperitoneal injections, mice were imaged using the Xenogen Spectrum (IVIS-Spectrum 200) imaging system and images were analysed using Living Image Software v4.6 (PerkinElmer).

Anti-PDGFRα neutralizing antibody treatment. NSG mice were implanted with 10,000 D458 Luc-ZsGreen cells into the lateral ventricle using a stereotaxic apparatus and the coordinates described above. BLI was performed to monitor early tumour engraftment. Slow-release buprenorphine was administered subcutaneously at 1.2 mg kg⁻¹ on the day of antibody treatment, 10 days after tumour implantation. Xenografted mice were randomly assigned to control and anti-PDGFRα antibody treatment groups. Using a stereotaxic apparatus and the coordinates described above, 5 µg of normal goat IgG (R&D Systems cat. no. AB-108-C) and 5 µg of goat anti-PDGFRα (R&D Systems cat. no. AF1062) was administered using a Hamilton needle (3 µl total volume) into the lateral ventricle of each control and treatment group mouse, respectively. The mice were closely monitored using BLI and for evidence of tumour burden. At the humane endpoint, the mice were euthanized for survival analysis.

MB cell lines
All experimental procedures were performed in accordance with the research ethics board at the Hospital for Sick Children (Toronto, Ontario). D458 (6–7-year-old male MB tumour; RRID: CVCL_1161)[42] was kindly provided by the Anindya Bagchi laboratory, Sanford Burnham Prebys. MB411 (or Med-411FH; 3-year-old male MB tumour) and MB813 (or Med-813FH; 2.6-year-old male MB tumour) patient-derived xenograft lines were obtained from the Brain Tumor Resource Lab (Jim Olsen, Seattle Children's Hospital)[43]. Cell lines were authenticated by short tandem repeat profiling and tested negative for mycoplasma contamination.

scRNA-seq
Cell dissociation and 10x Genomics. Mouse brain tumours and microdissected spinal meninges were incubated in 1 ml of 1× phosphate-buffered saline (PBS) with 0.41 U ml⁻¹ Liberase Research Grade (Roche cat. no. 5401119001) and 60 U ml⁻¹ DNase (Roche cat. no. 11284932001) for 1 h at 37 °C on an orbital shaker. Meningeal pellets were resuspended in 1 ml of 1% bovine serum albumin (BSA) and 120 µl of myelin removal beads II (Miltenyi Biotec cat. no. 130-096-433) and incubated at 4 °C for 15 min, with rocking. Meningeal samples were placed in a magnetic separator for 3 min. The supernatant was removed and spun down. Cell pellets were rinsed once in 1% BSA and processed for 10x Genomics. The cell count and viability of the single-cell suspension was assessed with trypan blue and a haemocytometer. Approximately 10,000–14,000 cells were loaded on to the Chromium Controller to capture single cells using the gel beads-in-emulsion approach. Gel beads-in-emulsion reverse transcription and cDNA amplification steps were performed using the Chromium Single Cell 3′ Gel Bead kit (cat. no. PN-1000121). Single-cell libraries with indices and Illumina P5/P7 adapters were generated using the Chromium Single Cell

3′ Library kit and the Chromium i7 Multiplex kit (cat. no. PN-1000077). The size, quality, concentration and purity of the cDNAs and the corresponding 10x library were assessed by the Agilent 2100 Bioanalyzer system. The 10x libraries were sequenced using the Illumina NovaSeq 6000 sequencing platform.

Alignment and preprocessing. scRNA-seq samples were aligned using CellRanger (version 3.1.0) to mouse reference mm10 with default settings. Each sample was preprocessed individually with the Seurat pipeline and filtered (features >400, percent.mt cut-off based on interquartile range) and doublets identified by DoubletFinder_v3 (ref. 44). Filtered samples were then combined with Seurat and batch correction for sample and cohort integration was applied with Harmony (theta 0). Single-cell data were normalized with the Seurat SCTransform workflow[45] and regularized negative binomial regression[46] with mitochondrial percentage and difference between the G2M and S phase scores regressed out. Principal components to use for nearest-neighbours analysis and Unifold Manifold Approximation and Projection (UMAP) dimension reduction were selected using a quantitative elbow plot approach (https://hbctraining.github.io/scRNA-seq/lessons/elbow_plot_metric.html).

Cell type annotation and comparisons. Clusters were identified with default Seurat Louvain algorithm and cluster markers were identified with Model-based Analysis of Single-cell Transcriptomics (MAST) test with 0.25 log fold change threshold, 0.1% expression threshold and minimum 10% expression in cluster and top markers were selected by log fold change. Clusters were annotated on the basis of published markers and matching to SingleR databases[47]. Differences in cluster proportions were analysed by dividing the number of cells in the cell type of interest by the total number of cells in the sample or the sample microenvironment fraction.

Differential expression analysis. Differential expression between samples based on tissue and genotype within clusters was performed with the MAST test with 0.25 log fold change threshold, 0.1% expression threshold and minimum 10% expression in cluster, followed by pathway analysis with the gprofiler2 package[48] with g:Profiler's Significance Correction Strategy (gSCS) threshold of 0.1.

Pathway enrichment analysis. We performed three integrative pathway enrichment analyses between differentially expressed genes of different cell types from primary tumour, metastatic leptomeninges and control leptomeninges using the ActivePathways (version 2.0.5) data fusion approach[49]. Differentially expressed genes were derived from scRNA-seq cluster comparisons. Genes that were considered characteristic to distinguishing cell types were used as the differentially expressed genes in the pathway enrichment. For each cell type, *P* values for differentially expressed genes that were not used to distinguish that cell type were set to 1 before ActivePathways analysis. Gene sets comprising the mouse biological processes of Gene Ontology and molecular pathways of Reactome were used for enrichment analysis and were downloaded from the g:Profiler web server (10 February 2025)[40]. Gene sets with at least 50 and no more than 750 genes were included in the enrichments analysis. Results from ActivePathways enrichment analysis were adjusted for multiple testing, and significant pathways were selected using default parameter settings (Holm family-wise error rate (FWER) <0.05). Enrichment maps were built in Cytoscape (version 3.10.1) using the EnrichmentMap app (version 3.3.6) and subsequently manually curated for functional themes using standard protocols[50].

Cell signalling analysis. Cell signalling analysis was performed by subsetting the samples of interest by tissue and genotype then running the CellChat algorithm for analysis of single-cell cross-talk using the built-in mouse database with default settings as suggested in the package tutorial, and significant interactions (using the permutation bases significance test) were visualized with CellChat functions as well[25].

CAF signatures. CAF signatures were scored with the Seurat AddModuleScore function and generated as follows: General_CAF = c('Pdgfra', 'Pdgfrb'); Antigen_presenting_CAF = c('H2-Aa', 'H2-Ab1', 'Cd74'); Inflammatory_CAF = c('Cxcl1', 'Cxcl2', 'Cxcl12', 'Ccl2', 'C1qa', 'C1qb', 'C1qc'); Myofibroblastic_CAF = c('Col1a1', 'Col4a1', 'Tgfb1').

Lentiviral production and transduction

The following lentiviral plasmids were designed using VectorBuilder as follows: pLV[Exp]-CMV>mCherry(ns):T2A:Bsd; pLV[Exp]-CMV>TagBFP2(ns):T2A:Bsd; pLV[Exp]-CMV > {hBMPR1A [NM_004329.3] Q233D(ns)}:T2A:TagBFP2(ns):P2A:Bsd; pLV[Exp]-CMV>hPDGFA[NM_002607.6] (ns):T2A:TagBFP2(ns):P2A:Bsd; pLV[Exp]-CMV>TurboGFP(ns):T2A:Luc2(ns):F2A:Neo (GFP-Luc). pHIV-Luc-ZsGreen (Luc-ZsGreen) was a gift from Bryan Welm (Addgene plasmid #39196). To produce lentiviral particles, 8×10^6 HEK-293T cells (ATCC cat. no. CRL-1573) were seeded in a 15-cm adherent plate with 30 ml of DMEM + 10% foetal bovine serum for 24 h and co-transfected with 10 µg lentiviral plasmid, 7.5 µg pMDLg (Addgene cat. no. 12251), 7.5 µg pRSV-Rev (Addgene cat. no. 12253) and 5 µg pMD2.G/VSVG (Addgene cat. no. 12259) using X-tremeGene 9 DNA transfection reagent (Roche cat. no. 6365779001). The supernatants containing the lentiviral particles were collected at 72 h after transfection and concentrated using Lenti-X concentrator (Clontech cat. no. 631231) and incubated at 4 °C overnight. Pellets were centrifuged at 1,500*g* for 45 min and resuspended in 1/100 of the original volume using 1× PBS dilution and stored at −80 °C. MB tumour lines (MB411, D458 and MB813) were transduced for 24 h and sorted for GFP, BFP and mCherry positivity (propidium iodide (PI) or 4′,6-diamidino-2-phenylindole (DAPI) as viability dyes) using the Sony MA900 at the SickKids-UHN Flow Cytometry Facility as described below.

Fluorescence-activated cell sorting

For MB-MAF co-implantation studies, mouse brain tumours and microdissected spinal meninges were incubated in 1 ml of 1× PBS with 0.41 U ml⁻¹ Liberase Research Grade (Roche cat. no. 5401119001), 60 U ml⁻¹ DNase (Roche cat. no. 11284932001) and 1× collagenase/dispase (Roche cat. no. 10269638001) for 1 h at 37 °C on an orbital shaker. Samples were spun at 300*g* for 10 min, and the supernatant was removed. Brain tumour pellets were resuspended in FACS buffer (1% BSA, 1 mM EDTA in 1× PBS) and filtered through a 40-µm strainer. Meningeal pellets were resuspended in 1 ml of FACS buffer. Then, 120 µl of myelin removal beads II (Miltenyi Biotec cat. no. 130-096-433) was added to the meningeal samples and incubated at 4 °C for 15 min, with rocking. The meningeal samples were briefly spun down and placed in a magnetic separator for 3 min. The supernatant was transferred to 1.5-ml tubes and spun down at 300*g* for 5 min. The meningeal samples were rinsed two times and blocked in 100 µl of 0.5 mg ml⁻¹ rat anti-CD16/CD32 (Thermo Fisher cat. no. 14-0161-82; lot no. 2083493) in FACS buffer at 4 °C for 10 min. Meningeal samples and Anti-Rat Ig, κ/Negative Control Compensation Particles Set (BD Biosciences cat. no. 552844) were incubated in the following antibody dilutions for 30 min at 4 °C in FACS buffer: BV421 anti-mouse CD31 (BD Biosciences cat. no. 563356; lot no. 9352427; 1:100), BV570 anti-mouse CD45 (BioLegend cat. no. 103135; lot no. B363153; 1:100), PE-Cy7 PDGFRA (Thermo Fisher cat. no. 25-1401-82; lot no. 1998291; 1:300) and APC anti-mouse CD146 (BioLegend cat. no. 134711; lot no. B375264; 1:100 for beads and 1:300 for samples). Samples were rinsed once in FACS buffer before resuspending in FACS buffer with propidium iodide (BD Biosciences cat. no. 556463; 1:1,000) before sorting. For fluorophore-labelled MB cells, cells were collected and spun down at 300*g*. The cell pellet was washed once in 1× PBS and dissociated using 1–2 ml of Accutase (STEMCELL Technologies cat. no. 07922) at room temperature for 5 min.

Dissociated cells were washed twice in FACS buffer and resuspended in FACS buffer containing PI or DAPI (Sigma-Aldrich cat. no. MBD0015; 1:3,000) before sorting. MB and fibroblast cells were sorted using Sony MA900 cell sorter (Model Type LE-MA900FP) with Cell Sorter Software v3.1.1 and equipped with 405-nm, 488-nm, 561-nm and 638-nm lasers and 525/30, 617/30, 785/60, 450/50, 585/30 and 665/30 bypass filters at the SickKids-UHN Flow Cytometry facility. Forward scatter area and back scatter area (FSC-A/BSC-A) gating was used to determine cells from debris and cell aggregates or doublets were removed by forward scatter width and height (FSC-W/FSC-H) followed by back scatter width and area (BSC-W/BSC-A). All staining was confirmed with unstained, single stain and/or PE-Cy7 PDGFRA FMO controls. PDGFRA$^+$ fibroblasts were determined and sorted as live (PI$^-$)/GFP$^-$/CD146$^-$/CD45$^-$/CD31$^-$/PDGFRA$^+$ cells (as described in Fig. 7; see also Supplementary Data 1 for full gating strategy). Flow cytometry plots were analysed and generated using FlowJo v10.8.0.

Immunofluorescence

For all IF procedures, mice were intracardially perfused with 30 ml of 1× PBS. For primary tumour and spinal cord sections, samples were fixed in 4% paraformaldehyde for 24 h at 4 °C, rinsed five times in 1× PBS, transferred to 15% sucrose in 1× PBS for at least 24 h at 4 °C and then transferred to 30% sucrose in 1× PBS for at least 24 h at 4 °C before embedding in optical cutting temperature (OCT) compound (Fisher Scientific cat. no. 23-730-571) on dry ice. OCT blocks were stored at −80 °C until sectioning tissue on to Fisherbrand Superfrost Plus Microscope slides (Fisher Scientific cat. no. 22-037-246) at a 16-µm thickness using a cryostat. Slides were stored at −80 °C until IF procedures. For tissue section IF, the slides were dried at room temperature for 10 min. Borders around the samples were drawn using ImmEdge Hydrophobic Barrier PAP pen (Vector Laboratories cat. no. H-4000). Subsequent processing steps were performed in an immunostain moisture chamber. Samples were rinsed at least three times (5 min each) with PBTr (0.1% Triton X-100 in 1× PBS) and blocked for at least 1 h in 10% goat/donkey serum, 0.1% Triton X-100 in 1× PBS (blocking solution). Samples were incubated in primary antibodies overnight at 4 °C in blocking solution. Samples were rinsed at least six times (5 min each) with PBTr. Samples were incubated in secondary antibodies for 1 h at room temperature in blocking solution. Samples were rinsed at least six times (5 min each) before incubating in DAPI for 5 min. Samples were rinsed three times in 1× PBS before mounting in Dako mounting medium (Agilent cat. no. S302380-2).

For whole-mount meningeal IF, the meninges were microdissected from the spinal cords and fixed in 4% paraformaldehyde for 20 min. The meninges were rinsed at least five times in 1× PBS and stored at 4 °C. Before IF staining, the meningeal samples were rinsed once in 1× PBS and blocked in 5% BSA, 0.1% Triton in 1× PBS for at least 1 h at room temperature with rocking. Samples were incubated in primary antibodies overnight at 4 °C in 5% BSA, 0.1% Triton in 1× PBS. Meninges were rinsed five times in 1% BSA, 0.1% Triton in 1× PBS for at least 1 h with rocking. Samples were incubated in secondary antibodies for 1 h at room temperature in 5% BSA, 0.1% Triton in 1× PBS with rocking. Meninges were rinsed five times in 1% BSA, 0.1% Triton in 1× PBS for at least 1 h and incubated in DAPI (1:1,000) for 5 min. Meninges were rinsed three times in 1× PBS before mounting in Dako mounting medium.

All IF antibodies (primary and secondary antibodies) and dilutions are described in the Supplementary Note.

Microscopy and image analysis

IF slides were imaged using a Quorum Leica DMi8 spinning disk confocal microscope equipped with a Photometric Prime 95B camera and a 20× (numerical aperture (NA) 0.8) and 40× (oil; NA 1.1) objectives. The acquisition software used was Volocity v7. Figure 2f was imaged using a Nikon A1R point-scanning confocal microscope equipped with 2× GaAsP photomultiplier tube (PMT), high definition resonance scanner,

32-channel spectral PMT and a 10× (NA 0.5) objective and NIS-Elements v5.11.01 software. Z-stack images were acquired on the microscopes at the SickKids Imaging Facility and analysed using Imaris Bitplane 10.1.0 (Oxford Instruments) as described in the Supplementary Note. GFP tumour burden imaging and analysis is also described in the Supplementary Note.

Statistics and reproducibility

The statistics and *n* values used for each experiment are described in the figure legends. All experiments include a minimum of three replicates for statistical quantification. In the case of the IF experiments, a minimum of two samples were quantified, each with multiple measurements across the tissue. For single-micrograph figures, multiple images were analysed with similar results, with the exception of Fig. 2f, where the mouse model presents with varying degrees of metastasis. No data were excluded from the analyses. All replicates were successful, with the exception of the MB co-implantation experiment, where varying degrees of metastasis or low recovery of fibroblasts led to unsuccessful attempts. Data distribution was assumed to be normal, but this was not formally tested. No statistical methods were used to predetermine sample sizes, but our sample sizes are similar to those reported in previous publications[51–53]. Animals were assigned to groups based on genotype when appropriate or randomly when mice of the same genotype were split into groups. For animal experiments, the humane intervention points were determined by a person blinded to cohort assignments. However, data collection and analysis were not performed blind to the conditions of the experiments. In the case of IF, BLI and GFP burden quantifications, we ensured that the same acquisition and analysis settings were used for both control and experimental groups to avoid biases. Representative IF images were chosen on the basis of mean values. Statistics were performed using GraphPad Prism 8. Kaplan–Meier survival graphs were generated using GraphPad Prism 8, and log-rank (Mantel–Cox) tests were performed for statistical analyses.

Reporting summary

Further information on research design is available in the Nature Portfolio Reporting Summary linked to this article.

Data availability

The scRNA-seq data that support the findings of this study have been deposited in the Gene Expression Omnibus (GEO) under accession code GSE264326. Source data are provided with this paper. Additional source images for Fig. 2f–h and Extended Data Fig. 9a,b are available via figshare at https://doi.org/10.6084/m9.figshare.28637567 (ref. 54). All other data supporting the findings of this study are available from the corresponding author on reasonable request.

Code availability

No custom code was used to generate or process the data.

References

41. Fan, J. J. et al. A forward genetic screen identifies potassium channel essentiality in SHH medulloblastoma maintenance. *Dev. Cell* https://doi.org/10.1016/j.devcel.2025.01.001 (2025).

42. He, X. M. et al. Differentiation characteristics of newly established medulloblastoma cell lines (D384 Med, D425 Med, and D458 Med) and their transplantable xenografts. *Lab. Invest.* **64**, 833–843 (1991).

43. Brabetz, S. et al. A biobank of patient-derived pediatric brain tumor models. *Nat. Med.* **24**, 1752–1761 (2018).

44. McGinnis, C. S., Murrow, L. M. & Gartner, Z. J. DoubletFinder: doublet detection in single-cell RNA sequencing data using artificial nearest neighbors. *Cell Syst.* **8**, 329–337 (2019).

45. Hao, Y. et al. Integrated analysis of multimodal single-cell data. *Cell* **184**, 3573–3587 (2021).

46. Hafemeister, C. & Satija, R. Normalization and variance stabilization of single-cell RNA-seq data using regularized negative binomial regression. *Genome Biol.* **20**, 296 (2019).

47. Aran, D. et al. Reference-based analysis of lung single-cell sequencing reveals a transitional profibrotic macrophage. *Nat. Immunol.* **20**, 163–172 (2019).

48. Kolberg, L., Raudvere, U., Kuzmin, I., Vilo, J. & Peterson, H. gprofiler2—an R package for gene list functional enrichment analysis and namespace conversion toolset g:Profiler. *F1000Research* **9**, ELIXER-709 (2020).

49. Paczkowska, M. et al. Integrative pathway enrichment analysis of multivariate omics data. *Nat. Commun.* **11**, 735 (2020).

50. Reimand, J. et al. Pathway enrichment analysis and visualization of omics data using g:Profiler, GSEA, Cytoscape and EnrichmentMap. *Nat. Protoc.* **14**, 482–517 (2019).

51. Lee, J. J. Y. et al. ZIC1 is a context-dependent medulloblastoma driver in the rhombic lip. *Nat. Genet.* **57**, 88–102 (2025).

52. Visvanathan, A. et al. Early rhombic lip Protogenin(+ve) stem cells in a human-specific neurovascular niche initiate and maintain group 3 medulloblastoma. *Cell* **187**, 4733–4750 (2024).

53. Donovan, L. K. et al. Locoregional delivery of CAR T cells to the cerebrospinal fluid for treatment of metastatic medulloblastoma and ependymoma. *Nat. Med.* **26**, 720–731 (2020).

54. Abeysundara, N. & Taylor, M. D. Metastatic medulloblastoma remodels the local leptomeningeal microenvironment to promote further metastatic colonization and growth. *figshare* https://doi.org/10.6084/m9.figshare.28637567 (2025).

Acknowledgements

Author contributions

Conceptualization, N.A., A.R. and M.D.T.; methodology, N.A., A.R., V.F., A.B., J.R., X.W. and M.D.T.; Investigation, N.A., A.R., V.F., A.B., R.V.O., K.J., M.V. and W.O.; formal analysis, N.A., A.R., V.F. and A.B.; animal husbandry, H.W., L.Q., N.H., J.P., T.D., E.M. and H.S.; writing—original draft, N.A., A.R. and M.D.T.; writing—review and editing, N.A., A.R., V.F., M.G., J.N.R. and M.D.T.; visualization, N.A., A.R., V.F. and A.B.; project administration, C.D. and M.D.T.; resources, N.A., A.R., V.F., A.B., R.V.O., K.J., B.L., P.d.A., M.L., B.L.H., O.S., S.B., H.-K.M., J.F., C.N., A.V., J.Z., K.N., K.Y.Z., C.-H.G.L., C.G.E., H.L., T.J., F.N., V.R., J.R., X.W., X.H. and M.D.T.; funding acquisition, M.D.T., C.D. and N.A.; supervision, M.D.T. and X.H.

Competing interests

The authors declare no competing interests.

Additional information

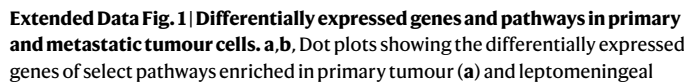**Extended data** is available for this paper at https://doi.org/10.1038/s41556-025-01660-7.

Supplementary information The online version contains supplementary material available at https://doi.org/10.1038/s41556-025-01660-7.

Correspondence and requests for materials should be addressed to Michael D. Taylor.
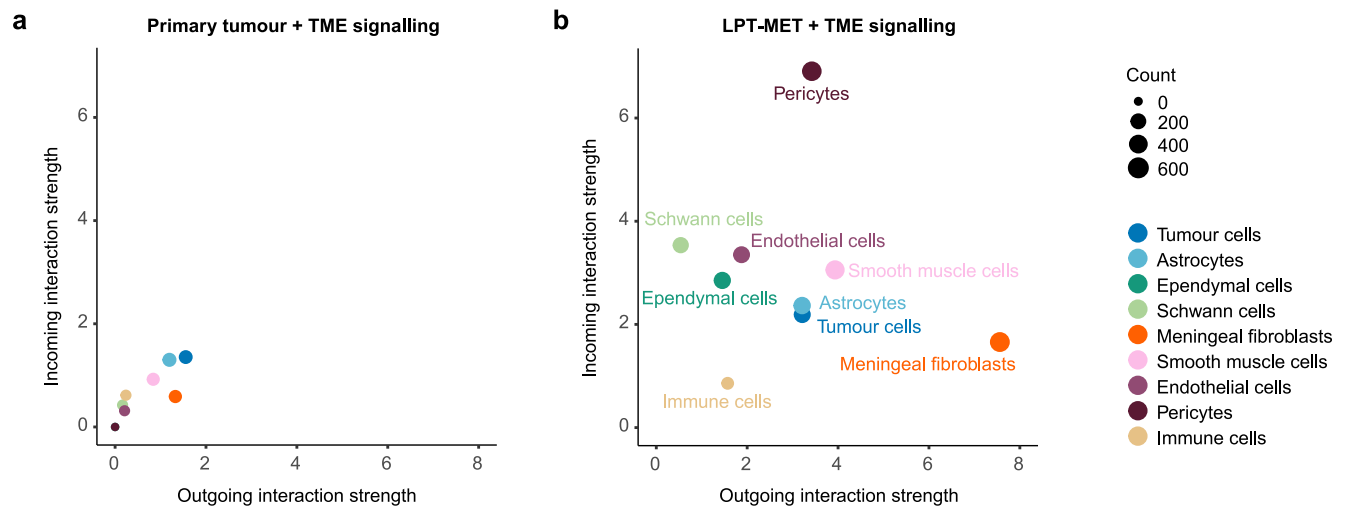
Peer review information *Nature Cell Biology* thanks Justin Lathia and the other, anonymous, reviewer(s) for their contribution to the peer review of this work.

Reprints and permissions information is available at www.nature.com/reprints.

Extended Data Fig. 1 | Differentially expressed genes and pathways in primary and metastatic tumour cells. a,b, Dot plots showing the differentially expressed genes of select pathways enriched in primary tumour (**a**) and leptomeningeal metastatic (LPT-MET) tumour (**b**) cells. *P* values were generated using a ranked hypergeometric test and corrected using the Holm-Bonferroni method of family-wise error rate (FWER). See Supplementary Table 1 for full gene list and pathways.
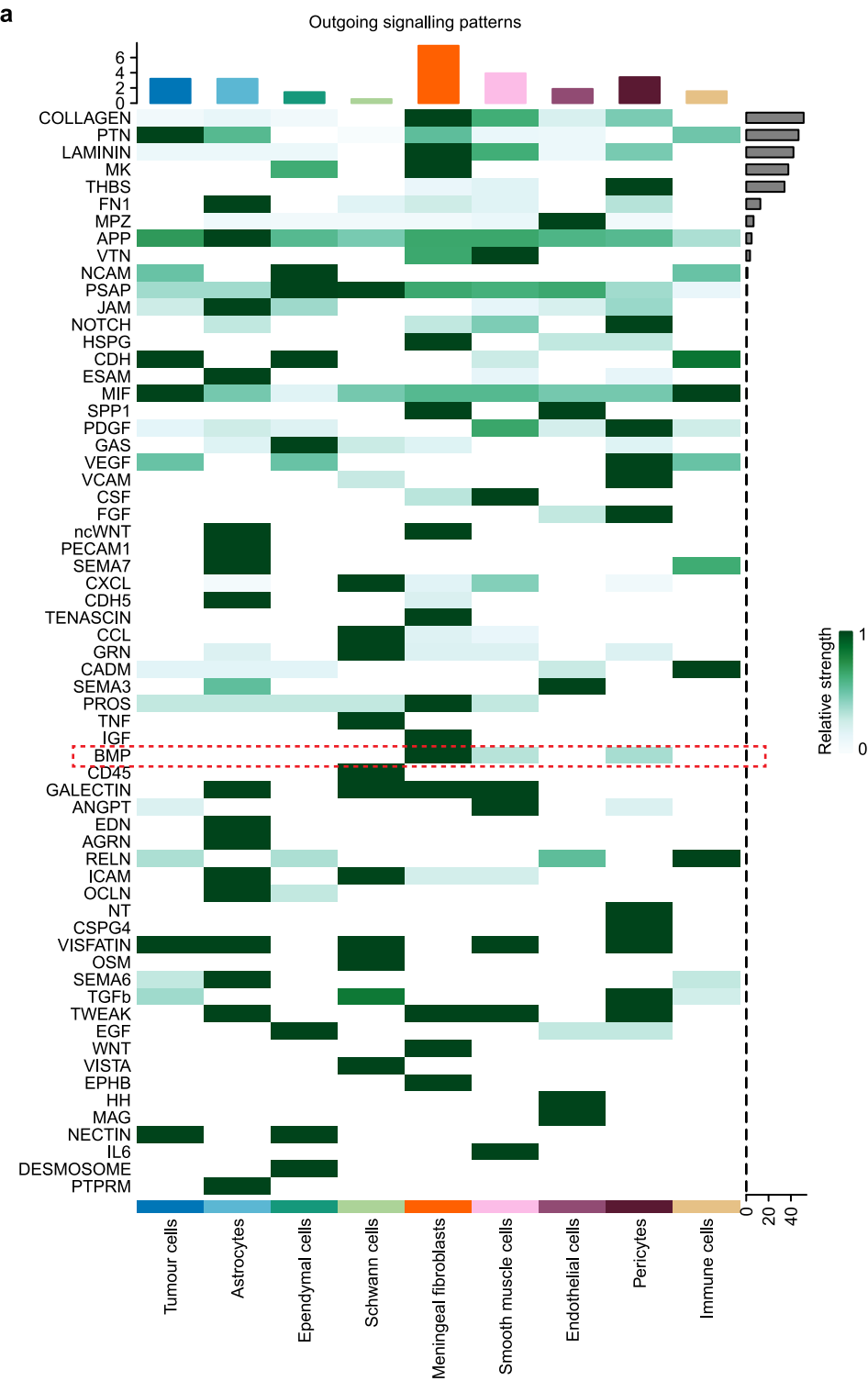
Extended Data Fig. 2 | Distinct intercellular signalling patterns within the primary tumour and metastatic niche. a,b, Plots are showing the cell populations from the primary tumour + TME (**a**) and LPT-MET + TME (**b**) scRNA-seq data with corresponding incoming interaction strength (y-axis) and outgoing interaction strength (x-axis) using CellChat. The interaction strength represents the total communication probability associated with each population and the count represents the number of inferred interactions.

Extended Data Fig. 3 | Meningeal fibroblasts as a major source of intercellular signalling. a, Heatmap showing the relative strength of outgoing signalling pathways from cell populations in the metastatic spinal leptomeninges using CellChat. BMP signalling is highlighted (red dashed box) as a pathway of significance to this study.
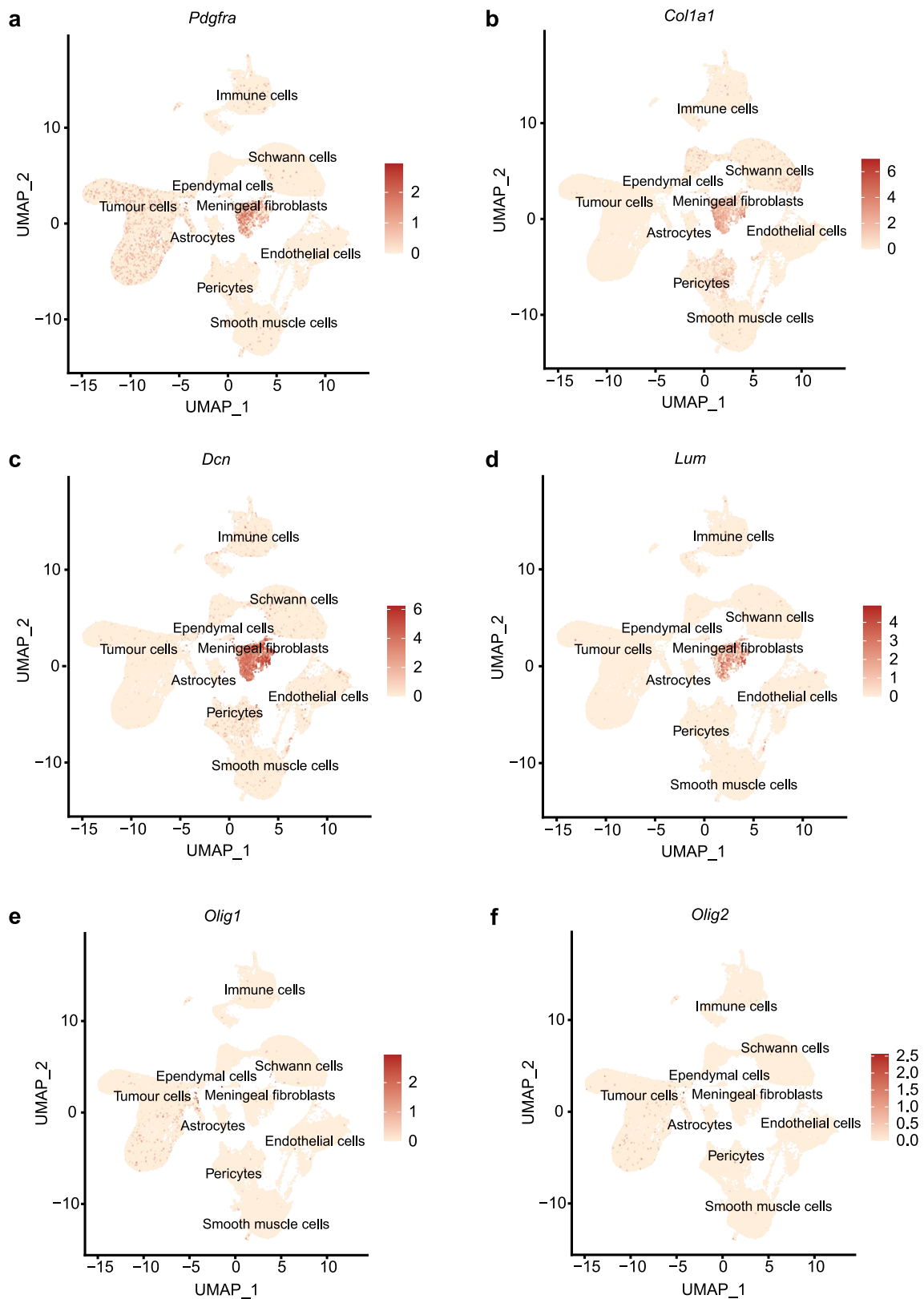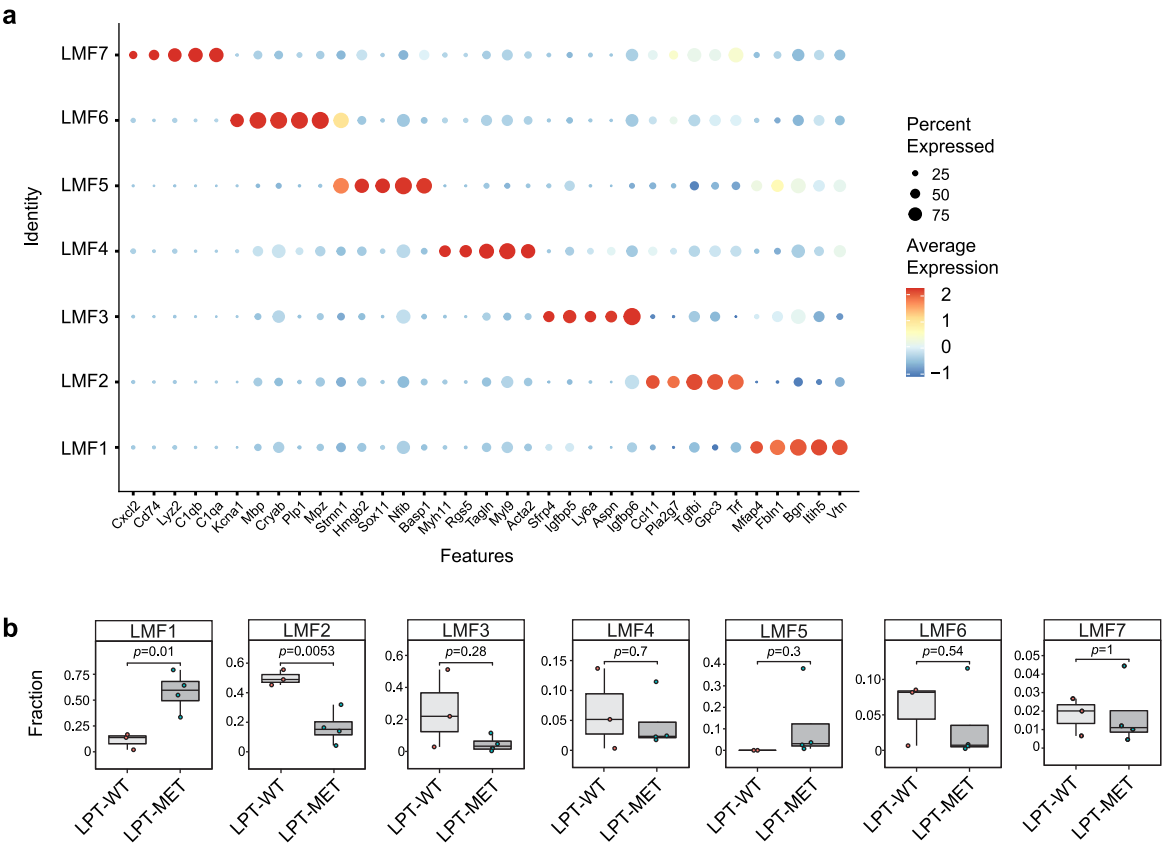
Extended Data Fig. 4 | Meningeal fibroblast and oligodendrocyte precursor cell markers. UMAP plots showing meningeal fibroblast markers *Pdgfra* (**a**), *Col1a1* (**b**), *Dcn* (**c**), and *Lum* (**d**), and OPC markers, *Olig1* (**e**) and *Olig2* (**f**), expression in LPT-WT and LPT-MET scRNA-seq datasets.
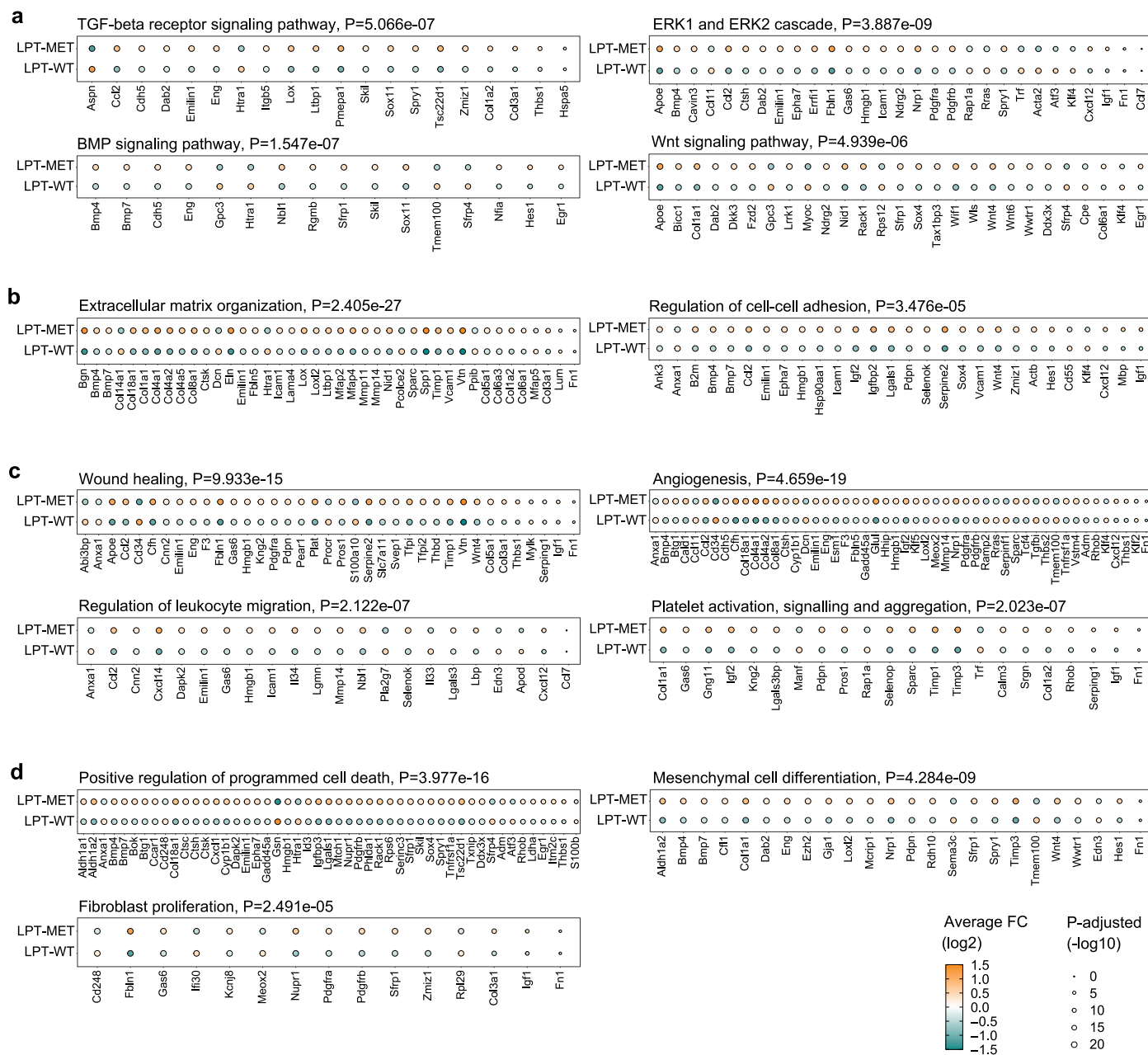
Extended Data Fig. 5 | Select pathways and differentially expressed genes in LPT-MET fibroblasts. Dot plots showing the differentially expressed genes associated with growth factor signalling (**a**), ECM organization and adhesion (**b**), immune and vasculature regulation (**c**), and cell death, differentiation, and proliferation (**d**) pathways in LPT-MET and LPT-WT meningeal fibroblasts. *P* values were generated using a ranked hypergeometric test and corrected using the Holm-Bonferroni method of family-wise error rate (FWER). See Supplementary Table 2 for full gene list and pathways.

a

b

Extended Data Fig. 6 | Meningeal fibroblast cluster markers and proportions. **a,** Dot plot showing the top five differentially expressed genes by Log Fold Change (MAST test, LFC >0.25, minimum percent expression >0.1) in meningeal fibroblasts from LPT-WT and LPT-MET samples. **b,** Box plots showing the LMF1-LMF7 mean cluster fractions per sample from LPT-WT (n = 3 mice) and LPT-MET (n = 4 mice) scRNA-seq data. Center line represents median (50% percentile), hinges represent the 25% and 75% percentile, and whiskers represent the 1.5 interquartile range. P values were generated using two-tailed Student's t-test.
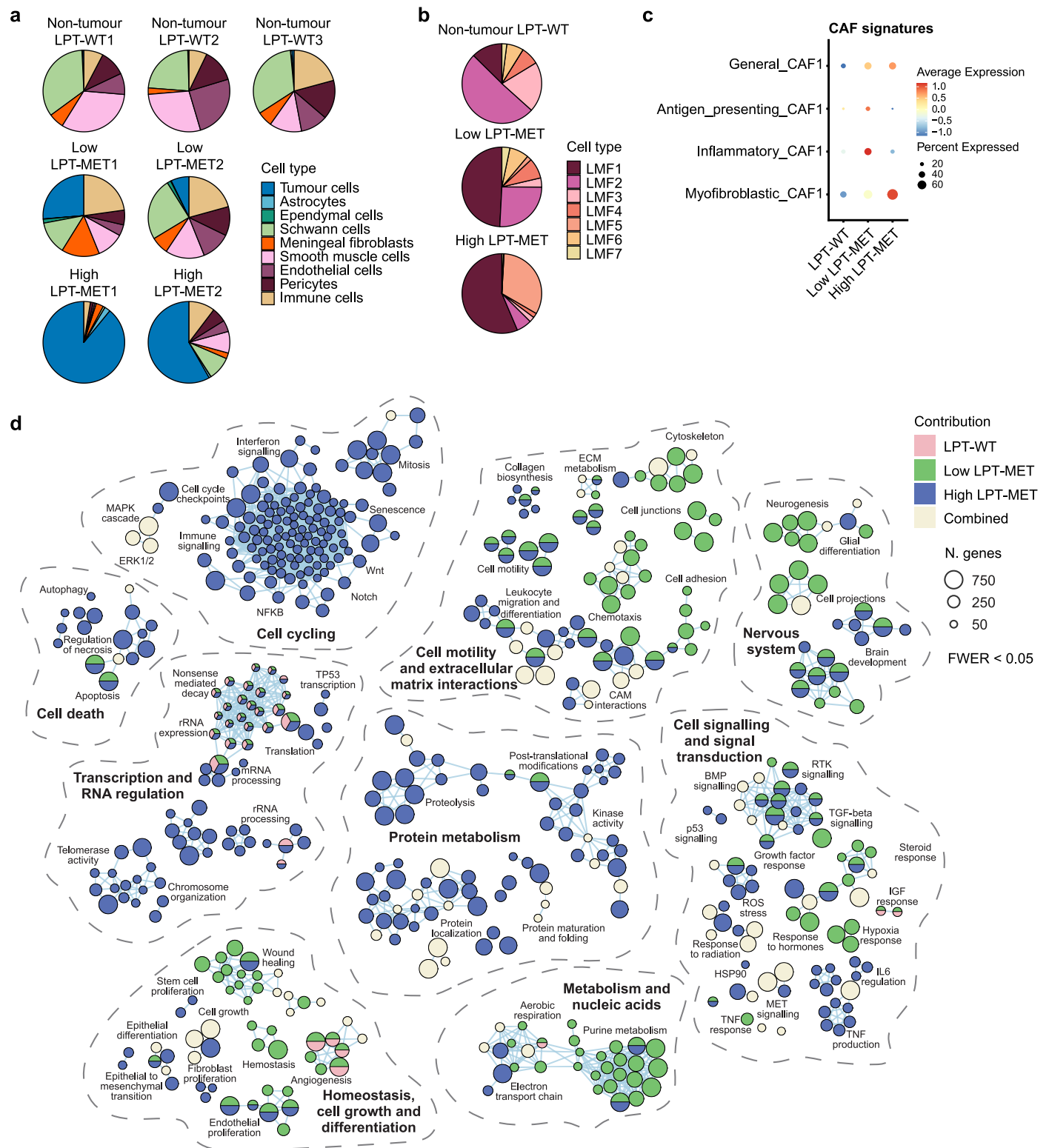
Extended Data Fig. 7 | Meningeal fibroblast cluster changes across metastatic leptomeningeal burden. a, Pie charts showing the proportion of cell populations within the leptomeningeal samples of non-tumour bearing Ptch-WT mice (non-tumour LPT-WT1, 2, 3) and Ptch-SB mice with low metastatic burden (Low LPT-MET1, 2), and higher metastatic burden (High LPT-MET1, 2). **b,** Pie charts showing the proportion of LMF1-LMF7 clusters within the meningeal fibroblasts associated with non-tumour LPT-WT, low LPT-MET, and high LPT-MET samples. **c,** Dot plot showing the Myofibroblastic, Inflammatory, Antigen presenting and General CAF signature expression in the meningeal fibroblasts associated with LPT-WT, low LPT-MET, and high LPT-MET samples. **d,** GO terms associated with the genes differentially expressed in the meningeal fibroblasts associated with LPT-WT, low LPT-MET, and high LPT-MET samples. The circle sizes correspond to the number of differentially expressed genes found in each pathway (Holm family-wise error rate (FWER) < 0.05). See Supplementary Table 3 for full gene list and pathways.
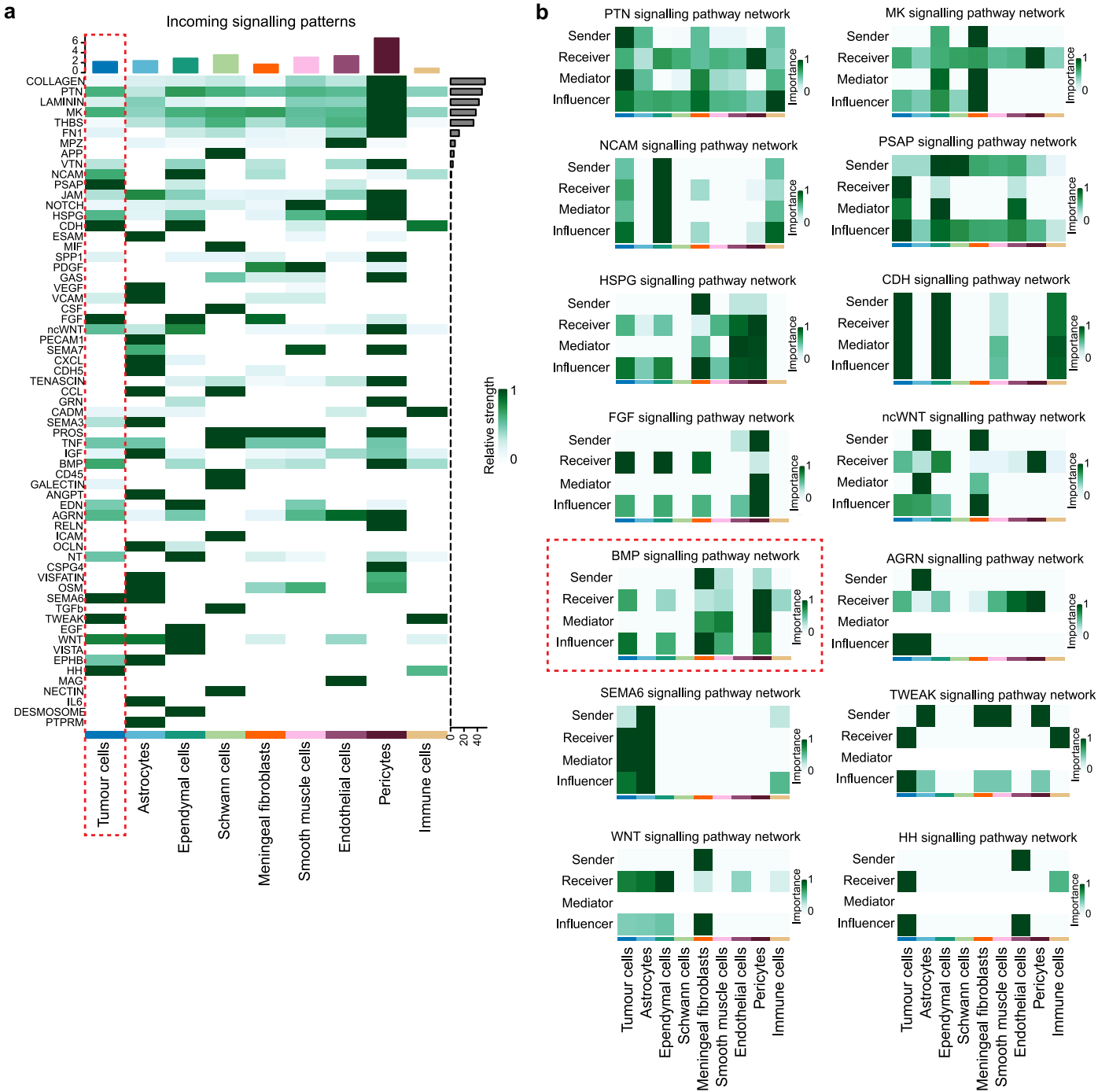
Extended Data Fig. 8 | Incoming signalling patterns in the metastatic leptomeninges. a, Heatmap showing the relative strength of incoming signalling pathways to cell populations in the LPT-MET samples using CellChat. The tumour-specific incoming signalling pattern column is outlined in the red dashed box. **b,** Heatmaps showing the relative importance of each cell group based on the computed four network centrality measures of select tumour-specific incoming signalling networks using CellChat. The BMP signalling network is highlighted in the red dashed box.
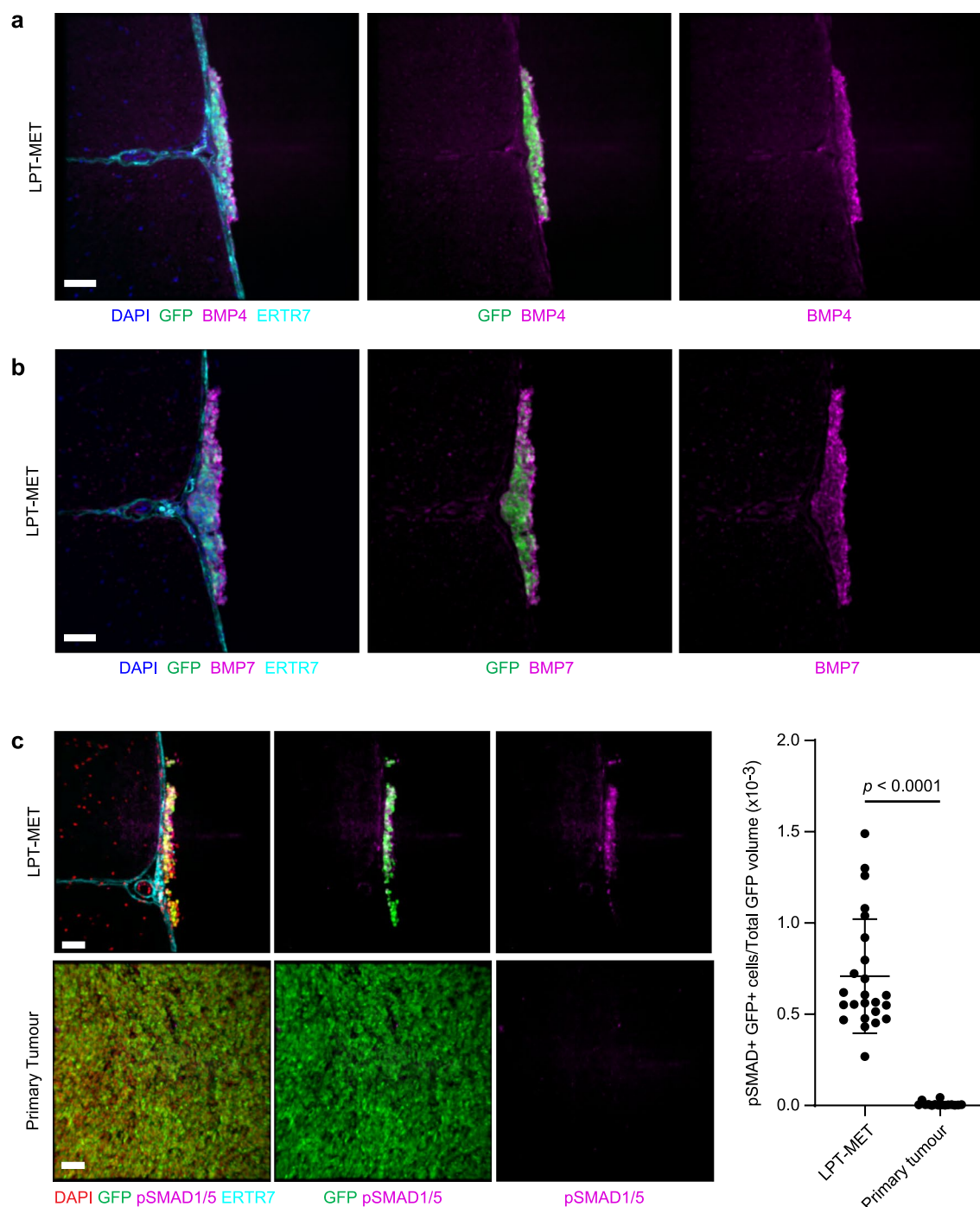
Extended Data Fig. 9 | BMP signalling in the SmoA1/Nestin-SB100/T2Onc2/ Math1-GFP mouse model. a,b, Spinal cord cross-sections fluorescently labelled with GFP+ tumour, ERTR7, DAPI, and BMP4 ($n = 18$ images) (**a**) or BMP7 ($n = 19$ images) (**b**). **c,** Spinal cord and primary tumour cross-sections fluorescently labelled with GFP, pSMAD1/5, ERTR7, and DAPI. The pSMAD- and GFP-double labelled positive cells normalized to total GFP volume was quantified in LPT-MET and primary tumour samples per field of view ($n = 15$ and $n = 24$ images for Primary tumour and LPT-MET, respectively). P value was generated using two-tailed unpaired t-test with Welch's correction, center line represents mean, and error bars represent standard deviation. Scale bars, 50 µm.
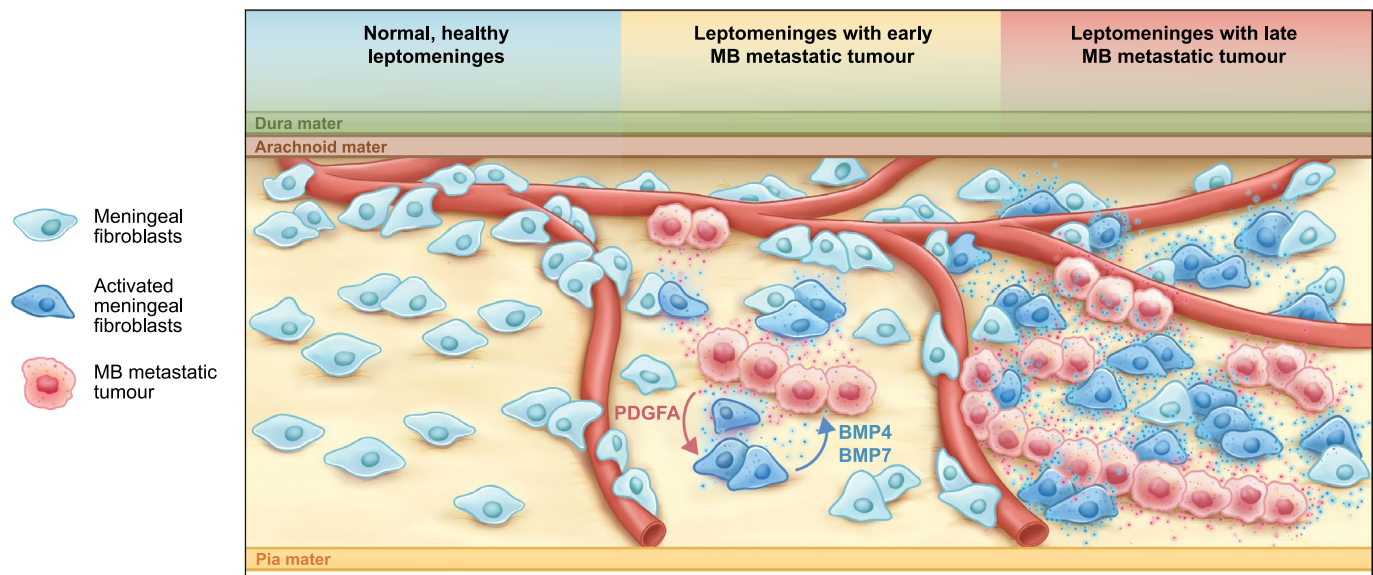
Extended Data Fig. 10 | Schematic summary of the normal and metastatic leptomeningeal niche. In the normal leptomeninges, meningeal fibroblasts are present and associate with meningeal blood vessels. In the presence of medulloblastoma (MB) metastatic tumour cells, secreted platelet-derived growth factor (PDGFA) ligands in the local microenvironment chemotactically recruit meningeal fibroblasts. Meningeal fibroblasts are reprogrammed to become MB-MAFs, expressing distinct transcriptomes and secretomes, including bone morphogenetic proteins 4 and 7 (BMP4/7). Active BMP and PDGF signalling further enhance both the colonization of the leptomeninges by MB cells as well as promoting the growth of established metastases.

nature portfolio

Corresponding author(s):   Michael D. Taylor

Last updated by author(s):   Mar 24, 2025

Reporting Summary

Nature Portfolio wishes to improve the reproducibility of the work that we publish. This form provides structure for consistency and transparency in reporting. For further information on Nature Portfolio policies, see our Editorial Policies and the Editorial Policy Checklist.

Statistics

For all statistical analyses, confirm that the following items are present in the figure legend, table legend, main text, or Methods section.

n/a	Confirmed	
☐	☒	The exact sample size (*n*) for each experimental group/condition, given as a discrete number and unit of measurement
☐	☒	A statement on whether measurements were taken from distinct samples or whether the same sample was measured repeatedly
☐	☒	The statistical test(s) used AND whether they are one- or two-sided *Only common tests should be described solely by name; describe more complex techniques in the Methods section.*
☐	☒	A description of all covariates tested
☐	☒	A description of any assumptions or corrections, such as tests of normality and adjustment for multiple comparisons
☐	☒	A full description of the statistical parameters including central tendency (e.g. means) or other basic estimates (e.g. regression coefficient) AND variation (e.g. standard deviation) or associated estimates of uncertainty (e.g. confidence intervals)
☐	☒	For null hypothesis testing, the test statistic (e.g. F, t, r) with confidence intervals, effect sizes, degrees of freedom and P value noted *Give P values as exact values whenever suitable.*
☒	☐	For Bayesian analysis, information on the choice of priors and Markov chain Monte Carlo settings
☒	☐	For hierarchical and complex designs, identification of the appropriate level for tests and full reporting of outcomes
☒	☐	Estimates of effect sizes (e.g. Cohen's *d*, Pearson's *r*), indicating how they were calculated

Our web collection on statistics for biologists contains articles on many of the points above.

Software and code

Policy information about availability of computer code

Data collection	ScRNA sequencing of mouse samples was performed using the Illumina NovaSeq 6000 platform and sequencing reads were aligned using CellRanger (v.3.1.0) to mouse reference mm10 with default settings. BLI was acquired using Xenogen Spectrum (IVIS-Spectrum 200) imaging system. IF images were acquired using a Quorum Leica DMi8 spinning disk confocal microscope with Volocity v7 software or a Nikon A1R point-scanning confocal microscope with NIS-Elements v5.11.01 software. GFP stereoscope images were acquired using Nikon SMZ25 stereomicroscope with NIS-Elements BR 5.02.00 software.
Data analysis	Computational analysis was performed with R (v4.0.3). scRNA-seq data was aligned with CellRanger (v3.1.0) and processed with the Seurat (v4.0.0) pipeline with Harmony (v1.0) batch effect correction and DoubletFinder (v2.0.3) for filtering out doubled cells. Differential expression analysis was performed with Seurat (v4.0.0) and pathway enrichment with gProfiler2 (v0.2.1). CellChat (v1.1.2) was used for tumour and microenvironment cross talk analysis. Integrative pathway enrichment analyses were performed using ActivePathways (v2.0.5) and enrichment maps were built in Cytoscape (v3.10.1) using EnrichmentMap app (v3.3.6). BLI was analyzed using Living Image Software v4.6 (PerkinElmer). Confocal analysis was performed using Imaris Bitplane v10.1.0 (Oxford Instruments) and GFP burden analysis was performed using ImageJ v1.54f (NIH, USA).

For manuscripts utilizing custom algorithms or software that are central to the research but not yet described in published literature, software must be made available to editors and reviewers. We strongly encourage code deposition in a community repository (e.g. GitHub). See the Nature Portfolio guidelines for submitting code & software for further information.

Data

All manuscripts must include a data availability statement. This statement should provide the following information, where applicable:

- Accession codes, unique identifiers, or web links for publicly available datasets
- A description of any restrictions on data availability
- For clinical datasets or third party data, please ensure that the statement adheres to our policy

The scRNA-seq data that support the findings of this study have been deposited in the Gene Expression Omnibus (GEO) under accession code GSE264326. Statistical source data is included for box plots, IF, BLI, GFP tumour burden, and survival data, with exact p-values. Additional source images for Fig. 2f, 2g, 2h, and Extended Data Fig. 9a, 9b are available through FigShare (https://doi.org/10.6084/m9.figshare.28637567). All other data supporting the findings of this study are available from the corresponding author on reasonable request.

Research involving human participants, their data, or biological material

Policy information about studies with human participants or human data. See also policy information about sex, gender (identity/presentation), and sexual orientation and race, ethnicity and racism.

Reporting on sex and gender	No patient-derived lines were generated in this study. No human participants were used in this study. All MB cell lines used in this study were generated and described elsewhere (He, X.M. et al. Lab Invest. 64, 833-43(1991); Brabetz, S. et al. Nature Medicine 24, 1752-1761(2018)).
Reporting on race, ethnicity, or other socially relevant groupings	Race and ethnicity were not considered.
Population characteristics	N/A
Recruitment	N/A
Ethics oversight	This study obtained full ethics approval from the Hospital for Sick Children (REB 0020020238 and REB 1000055059).

Note that full information on the approval of the study protocol must also be provided in the manuscript.

Field-specific reporting

Please select the one below that is the best fit for your research. If you are not sure, read the appropriate sections before making your selection.

☒ Life sciences   ☐ Behavioural & social sciences   ☐ Ecological, evolutionary & environmental sciences

For a reference copy of the document with all sections, see nature.com/documents/nr-reporting-summary-flat.pdf

Life sciences study design

All studies must disclose on these points even when the disclosure is negative.

Sample size	No statistical methods were used to predetermine sample sizes but our sample sizes are similar to those reported in previous publications (Lee, J.J.Y. et al. Nature Genetics 57, 88-102 (2025); Visvanathan, A. et al. Cell 187, 4733-4750.e26 (2024); Donovan, L.K. et al. Nature Medicine 26, 720-731 (2020)).
Data exclusions	No data exclusions were considered.
Replication	All experiments include a minimum of three replicates for statistical quantification. In the case of IF experiments, a minimum of two samples were quantified, each with multiple measurements across the tissue. For single micrograph figures, multiple images were analyzed with similar results, with the exception of Fig. 2f, where the mouse model presents with varying degrees of metastasis. All replicates were successful, with the exception of the MB co-implantation experiment, where varying degrees of metastasis or low recovery of fibroblasts led to unsuccessful attempts.
Randomization	The allotment to study groups were either random or based on mouse genotypes when appropriate. The scRNA-seq data was collected from tumour-bearing mice (patched heterozygous mutants) at humane endpoint and control mice with the appropriate genotype (patched wild-type mice). For medulloblastoma cell line-based studies involving mice of the same genotype (NSG mice), the cells were injected into groups of randomized age-matched mice. For PDGFRA inhibition studies, xenografted mice were randomly assigned to control and anti-PDGFRA antibody treatment groups. For co-implantation studies, tumour-bearing mice were collected at humane endpoint and processed for cell sorting. The presence of metastasis was determined during sorting and fibroblasts were co-implanted with primary tumour cells into groups of randomized age-matched mice, if enough cells were recovered for a minimum of three replicates.
Blinding	For animal experiments, humane intervention points were determined by a person blinded to cohort assignments. However, data collection and analysis were not performed blind to the conditions of the experiments.

Reporting for specific materials, systems and methods

We require information from authors about some types of materials, experimental systems and methods used in many studies. Here, indicate whether each material, system or method listed is relevant to your study. If you are not sure if a list item applies to your research, read the appropriate section before selecting a response.

Materials & experimental systems

n/a	Involved in the study
☐	☒ Antibodies
☐	☒ Eukaryotic cell lines
☒	☐ Palaeontology and archaeology
☐	☒ Animals and other organisms
☒	☐ Clinical data
☒	☐ Dual use research of concern
☒	☐ Plants

Methods

n/a	Involved in the study
☒	☐ ChIP-seq
☐	☒ Flow cytometry
☒	☐ MRI-based neuroimaging

Antibodies

Antibodies used

Rabbit anti-Collagen I (Abcam Cat no. ab21286; Lot no. GR3429622-1; 1:100); Rabbit anti-Mouse Collagen IV (Bio-Rad Cat no. 2150-1470; Lot no. 161115; 1:200); Goat anti-PDGFRA (R&D System Cat no. AF1062; Lot no. HMQ0221101; 1:100); Rat anti-Mouse CD31 Clone MEC13.3 (BD Pharmingen Cat no. 553370; Lot no. 7257819; 1:100); Rabbit anti-Laminin (Sigma-Aldrich Cat no. L9393; Lot no. 067M4872V; 1:500); Rat anti-Ki67 Clone SolA15 (Invitrogen Cat no. 14-5698-82; Lot no. 2747806; 1:500); Rat anti-ER-TR7 (Santa Cruz Cat no. sc-73355; Lot no. J3019; 1:500); Rabbit anti-BMP4 (Abcam Cat no. ab39973; Lot no. GR3267050-2; 1:100); Rabbit anti-BMP7 (Abcam Cat no. 56023; Lot no. GR3265320-7; 1:100); Rabbit anti-pSMAD1/5 (Cell Signaling Cat no. 9516; Lot no. 9; 1:100); Rabbit anti-ID1 (BioCheck BCH-1/195-14; Lot no. RN-61580; 1:500); Rabbit anti-mCherry (Abcam Cat no. 167453; Lot no. 1024587-1; 1:100); Rat anti-mouse CD16/CD32 monoclonal antibody, Clone 93 (Invitrogen Cat no. 14-016-82; Lot no. 2083493); APC anti-mouse CD146 (BioLegend Cat no. 134712; Lot no. B375264); BV570 anti-mouse CD45, Clone 30-F11 (BioLegend Cat no. 103136; Lot no. B363153); BV421 rat anti-mouse CD31, Clone 390 (BD Biosciences Cat no. 563356; Lot no. 9352427); PE-Cyanine7 rat anti-mouse CD140a, Clone APA5 (Invitrogen Cat no. 25-1401-82; Lot no. 1998291); Goat anti-Rabbit Alexa Fluor 555 (Invitrogen Cat no. A-21428; Lot no. 2278425); Donkey anti-Rat Alexa Fluor 594 (Invitrogen Cat no. A-21209; Lot no. 2041649); Donkey anti-Goat Alexa Fluor 594 (Invitrogen Cat no. A-11058; Lot no. 1003216); Donkey anti-Rabbit Alexa Fluor 594 (Invitrogen A-21207); Donkey anti-Rabbit Alexa Fluor 647 (Invitrogen Cat no. A-31573; Lot no. 2752586); Goat anti-Rat Alexa Fluor 647 (Invitrogen Cat no. A-21247; Lot no. 2268323) (1:500).

Validation

Rabbit anti-Collagen I (Abcam Cat no. ab21286): Manufacturer tested applications include ELISA, WB, IHC, ICC/IF and cited by 158 publications. Antibody expression in the mouse spinal meninges was also demonstrated in the following publications: Dorrier, C.E. et al. CNS fibroblasts form a fibrotic scar in response to immune cell infiltration. Nature Neuroscience 24, 234-244 (2021); Nguyen, Q.L. et al. Vascular PDGFRA-alpha protect against BBB dysfunction after stroke in mice. Angiogenesis 24, 35-46 (2021).

Rabbit anti-Mouse Collagen IV (Bio-Rad Cat no. 2150-1470): Manufacturer tested applications include ELISA, IHC, IF and cited by 59 references. Antibody expression in the mouse perivascular space and meninges was also demonstrated in the following publications: Manberg, A. et al. Altered perivascular fibroblast activity precedes ALS disease onset. Nature Medicine 27, 640-646 (2021); Andrae, J. et al. A role for PDGF-C/PDGFRa signaling in the formation of the meningeal basement membranes surrounding the cerebral cortex. Biology Open 5, 461-474 (2016).

Goat anti-PDGFRA (R&D System Cat no. AF1062): Manufacturer tested applications include WB, flow cytometry, IHC, IC/IF and cited by 277 references. Antibody expression in the mouse perivascular space and meninges was also demonstrated in the following publication: Nguyen, Q.L. et al. Vascular PDGFRA-alpha protect against BBB dysfunction after stroke in mice. Angiogenesis 24, 35-46 (2021). Anti-PDGFRA inhibition studies were performed in the following studies: Taniguchi, E., et al. PDGFR-A is a therapeutic target in alveolar rhabdomyosarcoma. Oncogene 27, 6550–6560 (2008); Tang, Z., et al. Survival effect of PDGF-CC rescues neurons from apoptosis in both brain and retina by regulating GSK3beta phosphorylation. J Exp Med. 207, 867-80 (2010).

Rat anti-Mouse CD31 Clone MEC13.3 (BD Pharmingen Cat no. 553370): Manufacturer tested applications include WB, flow cytometry, IHC, IF and cited by 13 references. Antibody expression in the mouse meningeal blood vessels was also demonstrated in the following publications: Cha, J-H. et al. Prompt meningeal reconstruction mediated by oxygen-sensitive AKAP12 scaffoling protein after central nervous system injury. Nature communications 5, 4952 (2014); Goldmann, T. et al. Origin, fate and dynamics of macrophages at CNS interfaces. Nature Immunology 17, 797-805 (2016).

Rabbit anti-Laminin (Sigma-Aldrich Cat no. L9393): Manufacturer antibody enhanced validation and tested applications include IHC/IF and cited by 1567 references. Antibody expression in the mouse perivascular space and meninges was also demonstrated in the following publications: Goldmann, T. et al. Origin, fate and dynamics of macrophages at CNS interfaces. Nature Immunology 17, 797-805 (2016); Bifari, F. et al. Neurogenic radial glia-like cells in the meninges migrate and differentiate into functionally integrated neurons in the neonatal cortex. Cell Stem Cell 20, 360-373 (2017).

Rat anti-Ki67 Clone SolA15 (Invitrogen Cat no. 14-5698-82): Manufacturer and publication tested applications include WB, flow cytometry, IHC, ICC/IF and cited by 375 references.

Rat anti-ER-TR7 (Santa Cruz Cat no. sc-73355): Manufacturer tested applications include WB, flow cytometry, IF and cited by 102

references. Antibody expression in the mouse meninges was also demonstrated in the following publications: Ahn, J.H. et al. Meningeal lymphatic vessels at the skull base drain cerebrospinal fluid. Nature 572, 62-66 (2019); Mestre, H. et al. Periarteriolar spaces modulate cerebrospinal fluid transport into brain and demonstrate altered morphology in aging and Alzheimer's disease. Nature Communications 13, 3897 (2022).

Rabbit anti-BMP4 (Abcam Cat no. ab39973): Manufacturer tested applications include WB, ICC/IF and cited by 72 references. BMP4 antibody was validated in transgenic mice overexpressing BMP4 and cells with BMP4 siRNA in the following publication: Zhang, X. et al. BMP4 overexpression induces the upregulation of APP/Tau and memory deficits in Alzheimer's disease. Cell Death Discovery 7, 51 (2021).

Rabbit anti-BMP7 (Abcam Cat no. 56023): Manufacturer tested applications include WB, IHC, ICC/IF and cited by 45 references. Immunostaining of BMP7 was demonstrated in the following publication: Mae, S-I. et al. Combination of small molecules enhances differentiation of mouse embryonic stem cells into intermediate mesoderm through BMP7-positive cells. Biochemical and Biophysical Research Communications 393, 877-882 (2010).

Rabbit anti-pSMAD1/5 (Cell Signaling Cat no. 9516): Manufacturer tested applications include WB, flow cytometry, IF and cited by 464 references.

Rabbit anti-ID1 (BioCheck BCH-1/195-14): Manufacturer tested applications include ELISA, WB, and IHC. IF staining in mouse embryonic stem cells was demonstrated in the following publication: Malaguti, M. et al. Id1 stabilizes epiblast identity by sensing delays in nodal activation and adjusting the timing of differentiation. Developmental Cell 50, 462-477 (2019).

Rabbit anti-mCherry (Abcam Cat no. 167453): Manufacturer tested applications include WB, ICC/IF and cited by 266 references, including the following publication: Shi, Y. et al. Tumour-associated macrophages secrete pleiotrophin to promote PTPRZ1 signalling in glioblastoma stem cells for tumour growth. Nature Communications 8, 15080 (2017).

For cell sorting experiments, we used CD16/CD32 monoclonal antibody (clone 93) to block Fc receptor, CD45 antibody (clone 30-F11), and CD31 antibody (clone 390) as previously published: Tauriello, D.V.F. et al. TGFbeta drives immune evasion in genetically reconstituted colon cancer metastasis. Nature 554, 538-543 (2018).

APC anti-mouse CD146 (BioLegend Cat no. 134712): Manufacturer tested applications include flow cytometry and cited by 10 references, including the following publication: Grosse, L. et al. Defined P16High senescent cell types are indispensible for mouse healthspan. Cell Metabolism 32, 87-99 (2020). Cd146 was found to be expressed in the pericyte and smooth muscle cell populations in our scRNA-seq data of the spinal leptomeninges.

PE-Cyanine7 rat anti-mouse CD140a Clone APA5 (Invitrogen Cat no. 25-1401-82): Manufacturer tested applications include flow cytometry and cited by 54 references, including the following publication: Santini, M.P. et al. Tissue-resident PDGFRa+ progenitor cells contribute to fibrosis versus healing in a context- and spatiotemporally dependent manner. Cell Reports 30, 555-570 (2020).

The following secondary antibodies have been validated for IF according to manufacturer's website (Invitrogen, ThermoFisher Scientific): Goat anti-Rabbit Alexa Fluor 555 (Invitrogen Cat no. A-21428), Donkey anti-Rat Alexa Fluor 594 (Invitrogen Cat no. A-21209), Donkey anti-Goat Alexa Fluor 594 (Invitrogen Cat no. A-11058), Donkey anti-Rabbit Alexa Fluor 594 (Invitrogen A-21207), Donkey anti-Rabbit Alexa Fluor 647 (Invitrogen Cat no. A-31573), Goat anti-Rat Alexa Fluor 647 (Invitrogen Cat no. A-21247).

Eukaryotic cell lines

Policy information about cell lines and Sex and Gender in Research

Cell line source(s)	D458 (6-7 year old male medulloblastoma tumour; RRID: CVCL_1161) was kindly provided by Anindya Bagchi lab, Sanford Burnham Prebys. MB411 (or Med-411FH; 3 year old male medulloblastoma tumour) and MB813 (or Med-813FH; 2.6 year old male medulloblastoma tumour) patient-derived xenograft lines were obtained from the Brain Tumor Resource Lab (Jim Olsen lab, Seattle Children's Hospital). HEK293T cells were obtained from ATCC (CRL-1573).
Authentication	MB cell lines were authenticated by STR profiling.
Mycoplasma contamination	Cell lines were tested negative for mycoplasma contamination.
Commonly misidentified lines (See ICLAC register)	No commonly misidentified lines were used in this study.

Animals and other research organisms

Policy information about studies involving animals; ARRIVE guidelines recommended for reporting animal research, and Sex and Gender in Research

Laboratory animals	Ptch+/−/Math1-SB11/SB76/Math1-GFP (active SB) mice with primary brain tumours and spinal metastases and Ptch+/+/SB76 / Math1-GFP (inactive SB) non-tumour bearing, age-matched (12-28 weeks) control mice were processed for single-cell RNA sequencing. T2Onc2 /Nestin-SB1002 mice were crossed with Math1-GFP/SmoA1 to generate the transgenic mouse line SmoA1/ Nestin-SB100/T2Onc2/Math1-GFP with high MB penetrance and metastatic burden. MB cerebellar and leptomeningeal implantation experiments were performed using NOD.Cg-Prkdc scid Il2rg tm1Wjl /SzJ (NSG or NOD scid gamma; JAX stock #005557) mice at 4-10 weeks of age. Pdgfra-H2BeGFP (JAX stock #007669) mice were analyzed individually (12-24 weeks of age) and backcrossed into NOD scid gamma background for six generations for patient-derived xenograft experiments (4-10 weeks of age). All mice were housed at TCP and housing room conditions were maintained as follows: 12 hour light and 12 hour dark cycles (Lights on at 7am; Lights off at

7pm); Room temperatures at 21-23°C; Humidity levels between 40-60%. All mice received extruded food pellets (Inotiv Cat no. TD.2918X) and reversed osmosis water (acidified and UV light filtration) via Avidity Science recirculating system and sterile quick disconnect water valves. Cages were changed every 2 weeks (cage bottom with new bedding; wire bar hopper and filter lid). Nesting material and enrichment devices were transferred to the new cage and only changed when soiled or damaged.

Wild animals	The study did not involve wild animals.
Reporting on sex	No sex discrimination was followed.
Field-collected samples	The study did not involve samples collected from the field.
Ethics oversight	All animal breeding and procedures were reviewed and approved by The Centre for Phenogenomics' (TCP) Animal Care Committee (AUP 25-0100H and 26-0151H). TCP is certified by the Canadian Council on Animal Care under the Animals for Research Act of Ontario.

Note that full information on the approval of the study protocol must also be provided in the manuscript.

Plants

Seed stocks	*Report on the source of all seed stocks or other plant material used. If applicable, state the seed stock centre and catalogue number. If plant specimens were collected from the field, describe the collection location, date and sampling procedures.*
Novel plant genotypes	*Describe the methods by which all novel plant genotypes were produced. This includes those generated by transgenic approaches, gene editing, chemical/radiation-based mutagenesis and hybridization. For transgenic lines, describe the transformation method, the number of independent lines analyzed and the generation upon which experiments were performed. For gene-edited lines, describe the editor used, the endogenous sequence targeted for editing, the targeting guide RNA sequence (if applicable) and how the editor was applied.*
Authentication	*Describe any authentication procedures for each seed stock used or novel genotype generated. Describe any experiments used to assess the effect of a mutation and, where applicable, how potential secondary effects (e.g. second site T-DNA insertions, mosiacism, off-target gene editing) were examined.*

Flow Cytometry

Plots

Confirm that:

☒ The axis labels state the marker and fluorochrome used (e.g. CD4-FITC).

☒ The axis scales are clearly visible. Include numbers along axes only for bottom left plot of group (a 'group' is an analysis of identical markers).

☒ All plots are contour plots with outliers or pseudocolor plots.

☒ A numerical value for number of cells or percentage (with statistics) is provided.

Methodology

Sample preparation	For MB-MAF co-implantation studies: Mouse brain tumours and microdissected spinal meninges were incubated in 1ml of 1X PBS with 0.41U/ml Liberase TM Research Grade (Roche Cat no. 5401119001), 60U/ml DNase (Roche Cat no. 11284932001), and 1X Collagenase/Dispase (Roche Cat no. 10269638001) for 1 hour at 37°C on an orbital shaker. Samples were spun at 300 x g for 10 min and the supernatant was removed. Brain tumour pellets were resuspended in FACS buffer (1% BSA, 1mM EDTA in 1X PBS) and filtered through a 40μm strainer. Meningeal pellets were resuspended in 1ml of FACS buffer. 120μl of Myelin Removal Beads II (Miltenyi Biotec Cat no. 130-096-433) was added to the meningeal samples and incubated at 4°C for 15 minutes, with rocking. The meningeal samples were briefly spun down and placed in a magnetic separator for 3 minutes. The supernatant was transferred to 1.5ml tubes and spun down at 300 x g for 5 min. The meningeal samples were rinsed 2 times and blocked in 100μl of 0.5mg/ml Rat anti-CD16/CD32 (Thermo Fisher Cat no. 14-0161-82; Lot no. 2083493) in FACS buffer at 4°C for 10 minutes. Meningeal samples and Anti-Rat Ig, κ/Negative Control Compensation Particles Set (BD Biosciences Cat no. 552844) were incubated in the following antibody dilutions for 30 minutes at 4°C in FACS buffer: BV421 anti-mouse CD31 (BD Biosciences Cat no. 563356; Lot no. 9352427; 1:100), BV570 anti-mouse CD45 (Biolegend Cat no. 103135; Lot no. B363153; 1:100), PE-Cy7 PDGFRA (Thermo Fisher Cat no. 25-1401-82; Lot no. 1998291; 1:300), and APC anti-mouse CD146 (Biolegend Cat no. 134711; Lot no. B375264; 1:100 for beads and 1:300 for samples). Samples were rinsed once in FACS buffer before resuspending in FACS buffer with propidium iodide (BD Biosciences Cat no. 556463; 1:1000) prior to sorting. For fluorophore-labelled medulloblastoma cells: Cells were collected and spun down at 300 x g. The supernatant was removed and cells were washed in 1X PBS and spun down. The supernatant was removed and the cell pellet was dissociated using 1-2ml of Accutase (STEMCELL Technologies Cat no. 07922) at room temperature for 5 minutes. Dissociated cells were resuspended in FACS buffer (1% BSA, 1mM EDTA in 1X PBS) and spun down. Cells were washed twice in FACS buffer and resuspended in FACS buffer containing PI or DAPI (Sigma-Aldrich Cat no. MBD0015; 1:3000) prior to sorting.
Instrument	Sony MA900 Cell Sorter (Model Type LE-MA900FP).
Software	Cell sorting data was acquired using Cell Sorter Software v3.1.1 and plots were generated using FlowJo v10.8.0.

Cell population abundance

The proportion of PDGFRA+ fibroblasts ranged from 1-15% of the single live (PI-)/GFP-/CD146-/CD45-/CD31- cell population and the samples were sorted using semi-purity mode.

Gating strategy

FSC-A/BSC-A gating was used to determine cells from debris and cell aggregates or doublets were removed by FSC-W/FSC-H followed by BSC-W/BSC-A. All staining was confirmed with unstained, single stain, and/or PE-Cy7 PDGFRA FMO controls. PDGFRA+ fibroblasts were determined as Live (PI-)/GFP-/CD146-/CD45-/CD31-/PDGFRA+ cells.

☒ Tick this box to confirm that a figure exemplifying the gating strategy is provided in the Supplementary Information.